

# The initial conditions of star formation in the $\rho$ Ophiuchi main cloud: wide-field millimeter continuum mapping

F. Motte<sup>1,2\*</sup>, P. André<sup>1\*\*</sup>, and R. Neri<sup>3</sup>

<sup>1</sup> CEA, DSM, DAPNIA, Service d'Astrophysique, C.E. Saclay, F-91191 Gif-sur-Yvette Cedex, France

<sup>2</sup> LAOG, Observatoire de Grenoble, UJF, BP 53, F-38041 Grenoble Cedex 9, France

<sup>3</sup> IRAM, 300 rue de la Piscine, F-38406 St. Martin d'Hères, France

Received 12 August 1997 / Accepted 21 November 1997

**Abstract.** We present the results of an extensive 1.3 mm continuum mosaicing study of the  $\rho$  Ophiuchi central region obtained at the IRAM 30-m telescope with the MPIfR 19-channel bolometer array. The mosaiced field covers a total area of  $\sim 480$  arcmin<sup>2</sup>, corresponding to  $\sim 1$  pc<sup>2</sup> at a distance of 160 pc, and includes the DCO<sup>+</sup> dense cores Oph-A, Oph-B1, Oph-B2, Oph-C, Oph-D, Oph-E, and Oph-F. Our mosaic is sensitive to features down to  $N_{\text{H}_2} \sim 10^{22}$  cm<sup>-2</sup> in column density. It is consistent with, but goes significantly deeper than, previous dust continuum studies of the cloud. For the first time, compact circumstellar dusty structures around young stellar objects are detected simultaneously with more extended emission from the dense cores and the ambient cloud. Thus, it becomes possible to directly study the genetic link between dense cores and young stars.

The diffuse cloud emission is itself fragmented in at least 58 small-scale, starless clumps harboring no infrared or radio continuum sources in their centers. Most of these starless fragments are probably gravitationally bound and pre-stellar in nature. Nineteen of them exhibit a relatively flat inner intensity profile, indicating they are not as centrally condensed as the envelopes seen around the embedded (Class I and Class 0) protostars of the cloud. Ten other clumps appear to be sharply peaked, however, and may represent candidate 'isothermal protostars', i.e., collapsing cloud fragments which have not yet developed a central hydrostatic core. The  $\sim 6000$  AU fragmentation sizescale estimated from our  $\rho$  Oph 1.3 mm mosaic is consistent with the typical Jeans length in the DCO<sup>+</sup> cores and is at least five times smaller than the diameter of isolated dense cores in the Taurus cloud. In agreement with this short lengthscale for fragmentation, the circumstellar envelopes surrounding  $\rho$  Oph Class I and Class 0 protostars are observed to have finite sizes and to be significantly more compact than their Taurus counterparts.

The measured frequency distribution of pre-stellar clump masses is relatively shallow below  $\sim 0.5 M_{\odot}$ , being consistent with  $\Delta N/\Delta m \propto m^{-1.5}$ , but steepens to  $\Delta N/\Delta m \propto m^{-2.5}$  above  $\sim 0.5 M_{\odot}$ . This is reminiscent of the *stellar* initial mass

function (IMF), suggesting the clumps we detect may be the *direct progenitors of individual stars*. Our observations therefore support theoretical scenarios in which gravitational fragmentation plays a key role in determining the stellar mass scale and the IMF.

Finally, the presence of several remarkable alignments of young stars and starless clumps in the 1.3 mm dust continuum mosaic supports the idea that various external agents, such as a slow shock wave originating in the Sco OB2 association, have induced core fragmentation and star formation in at least part of the cloud.

**Key words:** ISM: individual objects: Rho Ophiuchi – circumstellar matter – ISM: clouds – ISM: structure – stars: formation

## 1. Introduction

Located only  $\sim 160$  pc from the Sun, the  $\rho$  Ophiuchi dark cloud is one of the most conspicuous regions where low-mass star formation is taking place (e.g. Wilking 1992 for a review). The  $\rho$  Oph cloud consists of two massive, centrally condensed cores, L1688 and L1689, from each of which a filamentary system of streamers extends to the north-east over tens of parsecs (e.g. Loren 1989). While only little star formation activity is observed in the streamers, the westernmost core, L1688, harbors a rich cluster of young stellar objects (YSOs) at various evolutionary stages and is distinguished by a high star-formation efficiency (SFE  $\gtrsim 20\%$ , Wilking & Lada 1983 – hereafter WL83). The present paper will be concerned with this main core, which is  $\sim 1$  pc  $\times$  2 pc in size. Both the gas/dust content and the embedded stellar population of L1688 have been extensively studied for more than two decades. The distribution of the low-density molecular gas was mapped in C<sup>18</sup>O(1–0) by WL83 with a 1.1' beam, revealing a ridge of high column density gas ( $A_V$  up to  $\sim 50 - 100$  mag) of mass  $\sim 550 M_{\odot}$  (see Fig. 3a below). Loren (1989) observed the entire cloud (including the streamers) in <sup>13</sup>CO(1–0) with a 2.4' beam and measured a total mass of  $\sim 3000 M_{\odot}$  for the complex. Maps of the higher density gas were made using molecular tracers such as SO, H<sub>2</sub>CO, NH<sub>3</sub>, HCO<sup>+</sup>, and DCO<sup>+</sup>, identifying several compact dense cores (labeled

Send offprint requests to: F. Motte

\* e-mail: fmotte@cea.fr

\*\* e-mail: pandre@cea.fr

Oph-A to Oph-F) inside the  $C^{18}O$  ridge (e.g. Loren & Wootten 1986, Loren, Wootten, & Wilking 1990 – hereafter LW90).

The dust continuum emission associated with some of these dense cores was mapped at 1.3 mm with an effective angular resolution of  $\lesssim 15''$  by Mezger et al. (1992b), in search of protostellar condensations. Oph-A, Oph-B1, Oph-B2, and part of Oph-F were positively detected, but only Oph-A revealed strong compact condensations while the other cores appeared structureless (we will see here that this is actually not the case). More recently, a half square degree centered on the main cloud was imaged in the mid-IR ( $6.75 \mu\text{m}$  and  $15 \mu\text{m}$ ) at  $6''$  resolution with the ISOCAM instrument aboard the ISO satellite, revealing many emission and absorption details on the dust spatial distribution (ISOCAM central-programme survey by Nordh, Olofsson et al. – see Abergel et al. 1996).

The stellar content of the  $\rho$  Oph cloud core has also been observed at wavelengths ranging between the X-ray and the radio band. In X-rays, *Einstein* and *ROSAT* surveys revealed  $\sim 70$  highly variable sources associated with magnetically-active young stars (Montmerle et al. 1983, Casanova et al. 1995). In the near-infrared, several surveys (e.g. Greene & Young 1992 – hereafter GY, Barsony et al. 1997, and references therein) discovered more than 200 low-luminosity embedded sources which have been divided into three classes interpreted as an evolutionary sequence (Class I  $\rightarrow$  Class II  $\rightarrow$  Class III) from (evolved) protostars to weak T Tauri stars (Lada 1987; Wilking, Lada, & Young 1989 – hereafter WLY). This empirical infrared classification scheme of the  $\rho$  Oph embedded cluster was generalized to all YSOs, and was used to support the ‘standard’ theory of low-mass star formation (Adams, Lada, & Shu 1987; Shu, Adams, & Lizano 1987). On the basis of (sub)millimeter dust continuum observations, the YSO classification scheme was then slightly revised and extended toward younger sources with the addition of the Class 0 early protostar stage (André, Ward-Thompson, & Barsony 1993 – hereafter AWB93; André & Montmerle 1994 – hereafter AM94). In the centimeter radio continuum range, several VLA surveys resulted in the discovery of more than 20 radio-emitting YSOs (e.g. Leous et al. 1991 – hereafter LFAM – and references therein).

Because of the wealth of data already obtained, the  $\rho$  Ophiuchi cloud may serve as a reference laboratory to which other regions of low-mass star formation can be compared. Since the details of the star formation process are likely to vary from cloud to cloud and to depend on environmental factors, it is crucial to study several regions in order to build a complete theoretical picture. The  $\rho$  Oph main cloud may offer both the nearest example of a region of induced star formation (e.g. Vrba 1977) and the nearest example of a young embedded cluster (WL83). It may thus be representative of the ‘clustered’ mode of star formation, which is probably the dominant mode in the Galaxy (e.g. Lada, Strom, & Myers 1993). In contrast, the Taurus-Auriga molecular cloud, which has a much lower spatial density of YSOs, is thought to be representative of a more quiescent, ‘isolated’ mode of low-mass star formation.

In the present paper, we discuss the results of a deep 1.3 mm continuum mapping study of the  $\rho$  Oph main cloud

obtained with the IRAM 30-m telescope equipped with the MPIfR bolometer array. Previous millimeter continuum studies were sensitive only to either the interstellar dust of dense cores (e.g. Mezger et al. 1992b) or the circumstellar dust of YSOs (e.g. AM94). Thanks to the improved sensitivity provided by bolometer arrays, we are here able to probe, for the first time, both cloud and circumstellar dust emission simultaneously. One of the motivations for this high angular resolution ( $11''$ ) work was to see whether the differences existing between  $\rho$  Ophiuchi and Taurus on large scales had direct consequences for the star formation process on circumstellar scales. The results of our mapping observations are described and compared with other existing data in Sect. 2 and Sect. 3. Sect. 4 presents an analysis of the radial intensity profiles of selected sources. In Sect. 5, we examine the nature and overall properties of the various small-scale structures detected in our maps. In Sect. 6, we relate these properties to larger-scale phenomena and discuss possible implications for our understanding of the processes of fragmentation and star formation in clusters. Our conclusions are summarized in Sect. 7.

## 2. Observations and data analysis

The 1.3 mm dust continuum emission from the  $\rho$  Oph central cloud was mapped with the IRAM 30-m telescope located near Granada, Spain, during four observing sessions between March 1995 and February 1997.

All of these runs (1995 March 17th to 21st, 1996 March 13th to 17th, 1996 April 3rd to 4th, 1997 February 17th to 23rd) were performed with the MPIfR 19-channel bolometer array (e.g. Kreysa 1992). Fifty on-the-fly maps were obtained with this array, corresponding to a total of 950 single-channel coverages. The effective field of view of each single-channel coverage varied from  $3' \times 1.5'$  to  $6.5' \times 3.5'$ . Such fields can be mapped in less than  $\sim 1$  hr with homogeneous observing conditions. The resulting mosaic of the  $\rho$  Oph main cloud (Fig. 1), which includes Oph-A, Oph-B1, Oph-B2, Oph-C, Oph-D, Oph-E, and Oph-F covers a total area of  $\sim 480 \text{ arcmin}^2$ , corresponding to  $\sim 1 \text{ pc}^2$ .

The individual on-the-fly maps were carried out in the dual-beam raster mode with a scanning velocity of  $4''/\text{sec}$  (or  $8''/\text{sec}$ ) and a sampling of  $2''$  (or  $4''$ ) in azimuth, a spatial sampling of  $4''$  in elevation, and a wobbler frequency of 2 Hz. In this observing mode, the telescope is scanned continuously in azimuth along each row while chopping. For each channel, the raw data corresponding to a single on-the-fly coverage consist of several rows (or scans) taken at a series of elevations. The wobbler throw (in azimuth) was usually set to  $44''$ , but  $32''$  was used for the smallest maps. As much as possible, the hour angle of each individual map was selected so as to avoid chopping into strong point sources (known from the YSO photometric survey of AM94) and to make the chopping/scanning direction roughly perpendicular to the long axis of the molecular cores in the field. The beam size was measured to be  $\sim 11''$  using Uranus and other strong point-like sources such as quasars. The absolute pointing of the telescope was checked every  $\sim 1$  hr

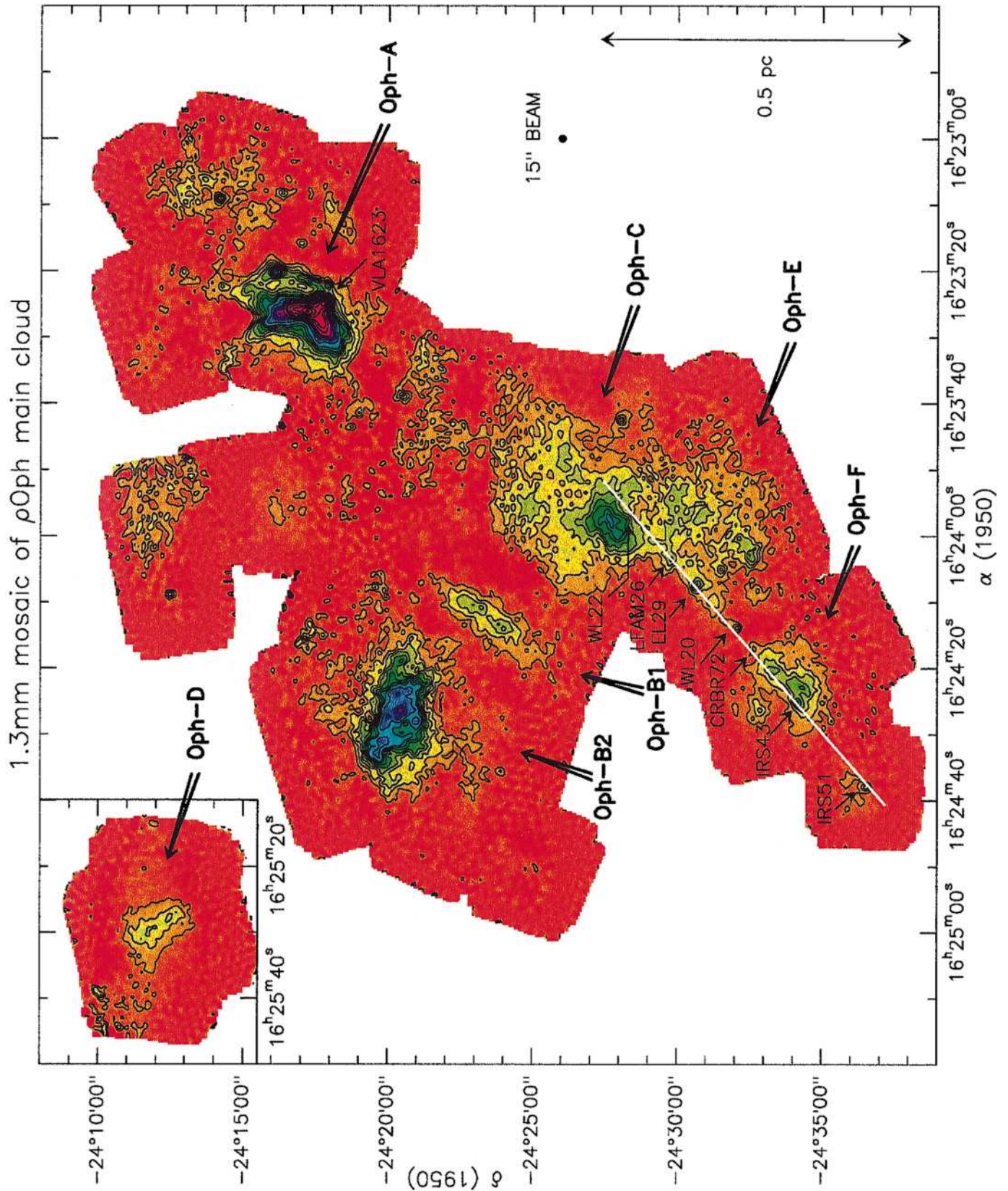


**Fig. 1.** Millimeter continuum mosaic of the  $\rho$  Oph main cloud including the dense cores Oph-A, Oph-B1, Oph-B2, Oph-C, Oph-D, Oph-E, and Oph-F. The data were smoothed to an effective angular resolution of  $15''$  (HPBW). The mosaic results from the combination of 50 on-the-fly coverages with the MPIfR 19-channel bolometer array and covers a total area of  $\sim 480$  arcmin $^2$ . Contour levels go from 5 to 40 MJy/sr with steps of 5 MJy/sr, from 50 to 80 MJy/sr by 10 MJy/sr, 100 MJy/sr and from 120 to 280 MJy/sr with steps of 40 MJy/sr (1 MJy/sr  $\simeq$  6 mJy/ $15''$ -beam). The mean rms noise level is  $\sim 1.2$  MJy/sr. Note the remarkable linear chain of clumps and embedded YSOs in the southern part of the ' $C^{18}O$  ridge' (emphasized by a white straight line).

and found to be accurate to better than  $\sim 3''$ – $5''$  (maximum deviation in both coordinates). In order to further improve the relative pointing accuracy within our mosaic, we recentered the individual maps assuming that the circumstellar structures detected around radio-emitting YSOs peak at the corresponding VLA positions (known to better than  $1''$  – see LFAM).

All of the data were taken at night or early morning and most of them benefited from good weather conditions. The zenith atmospheric optical depth, monitored by ‘skydips’ every 1–2 hr, was between  $\sim 0.1$  and  $\sim 0.4$ . Calibration was achieved through on-the-fly mapping and on-off observations of the primary calibrator Uranus (e.g. Griffin & Orton 1993 and references therein). In addition, the  $\rho$  Oph secondary calibrator IRAS 16293-2422, which has a 1.3 mm peak flux density  $\sim 5.3$  Jy in an  $11''$  beam (e.g. AM94) was observed before and after each map. The relative calibration was found to be good to within  $\sim 10\%$  by comparing the individual coverages of each field, and the overall absolute calibration uncertainty is estimated to be  $\sim 20\%$ . The passband of the bolometers used has an equivalent width  $\approx 70$  GHz and is centered at  $\nu_{eff} \approx 240$  GHz (e.g. Kreysa 1992).

The dual-beam maps were reduced with the new IRAM software for bolometer-array data (“NIC”; cf. Brogière, Neri, & Sievers 1995) which uses the EKH restoration algorithm (Emerson, Klein, & Haslam 1979). Zero-order baselines were subtracted from the data prior to restoration. A few maps taken in March 1996 suffered from strong skynoise and were processed using a noise-reduction algorithm that removes a correlated noise component from each channel, based on the signal seen by the other channels of the array (Brogière et al. 1995).

### 3. Results

The final, co-added 1.3 mm mosaic of  $\rho$  Oph main cloud is shown in Fig. 1 in the form of an isophotal contour map overlaid on a color-scale image. Remaining image artifacts resulting from unbalanced ‘dual-beam restoration’ were removed by smoothing the images to an effective beam resolution of  $13''$  ( $15''$  for the full mosaic). Blow-up 1.3 mm maps of the DCO<sup>+</sup> cores Oph-A, Oph-B1/B2, Oph-C, Oph-D, Oph-E, Oph-F, and of several new, more diffuse cores extracted from the mosaic of Fig. 1, are presented at  $13''$  angular resolution in Figs. 2a–2h.

The mean rms noise of these maps is  $\sim 8$  mJy per  $13''$  beam, but the rms noise at a given position varies from 4.5 mJy/ $13''$ -beam to 15 mJy/ $13''$ -beam depending on the local number of coverages and the corresponding observing conditions. Within the mosaic, the areas with best sensitivity (rms  $\sim 4.5$  mJy/ $13''$ -beam) are located around the starless cores Oph-C-S<sup>1</sup> (see Fig. 2c) and Oph-D (see Fig. 2d).

#### 3.1. Column densities

As millimeter dust continuum emission is generally optically thin, our bolometer maps should directly reflect the column den-

sity distribution within the mosaiced region. The beam-averaged column density along any given line of sight may be derived from the 1.3 mm flux density  $S_{1.3\text{mm}}^{\text{beam}}$  measured in a single (Gaussian) beam by:

$$\langle N_{\text{H}_2} \rangle_{\text{beam}} = S_{1.3\text{mm}}^{\text{beam}} / [\Omega_{\text{beam}} \mu m_{\text{H}} \kappa_{1.3\text{mm}} B_{1.3}(T_{\text{dust}})], \quad (1)$$

where  $\Omega_{\text{beam}}$  is the main beam solid angle,  $\mu = 2.33$  is the mean molecular weight,  $m_{\text{H}}$  is the mass of atomic hydrogen,  $\kappa_{1.3\text{mm}}$  is the dust opacity per unit mass column density at  $\lambda = 1.3$  mm, and  $B_{1.3}(T_{\text{dust}})$  is the Planck function for a dust temperature  $T_{\text{dust}}$ . In the Rayleigh-Jeans approximation of the Planck function, the above equation takes on the practical form:

$$\langle N_{\text{H}_2} \rangle_{\text{beam}} \approx 4 \times 10^{21} \text{ cm}^{-2} \times \left( \frac{S_{1.3\text{mm}}^{\text{beam}}}{10 \text{ mJy}/13''\text{-beam}} \right) \times \left( \frac{T_{\text{dust}}}{20 \text{ K}} \right)^{-1} \times \left( \frac{\kappa_{1.3\text{mm}}}{0.005 \text{ cm}^2 \text{ g}^{-1}} \right)^{-1}. \quad (1')$$

Converting column density  $N_{\text{H}_2}$  into visual extinction  $A_V$  using the relation  $A_V \sim 10^{-21} N_{\text{H}_2}$  (e.g. Bohlin, Savage, & Drake 1978), we see that the typical  $3\sigma$  detection threshold in Fig. 1 and Fig. 2 is  $\langle N_{\text{H}_2} \rangle_{\text{beam}} \sim 10^{22} \text{ cm}^{-2}$  or  $A_V \sim 10$ .

The main uncertainty in the above derivation (Eq. 1) arises from the dust opacity coefficient  $\kappa_{1.3\text{mm}}$  (see Henning, Michel, & Stognienko 1995 for a review). The dust temperature  $T_{\text{dust}}$  is also somewhat uncertain but less critical in this respect (e.g. AM94). Since we are interested in a variety of dust features including circumstellar material around young stars, pre-stellar dense clumps/cores, and diffuse interstellar cloud material, both  $\kappa_{1.3\text{mm}}$  and  $T_{\text{dust}}$  may be expected to vary over the extent of our maps. We have therefore adopted three values of the dust mass opacity:  $\kappa_{1.3\text{mm}} = 0.02 \text{ cm}^2 \text{ g}^{-1}$  for circumstellar disks around Class II sources (see, e.g., Beckwith et al. 1990 and Pollack et al. 1994),  $\kappa_{1.3\text{mm}} = 0.01 \text{ cm}^2 \text{ g}^{-1}$  for circumstellar envelopes around Class I and Class 0 protostars (Ossenkopf & Henning 1994, AM94), and  $\kappa_{1.3\text{mm}} = 0.005 \text{ cm}^2 \text{ g}^{-1}$  for pre-stellar dense clumps and cores (Preibisch et al. 1993, André, Ward-Thompson, & Motte 1996 – hereafter AWM96). In actual fact, the dust mass opacity is not discontinuous from one class of sources to the next, and there is probably little difference for instance between the dust in the outer parts of a circumstellar envelope and the dust in a pre-stellar core. Nevertheless, our adopted values should roughly track the real variations of  $\kappa_{1.3\text{mm}}$  (cf. Henning et al. 1995). The continuity between classes and the ambiguous classification of some objects imply a typical uncertainty of a factor of  $\sim 2$  on  $\kappa_{1.3\text{mm}}$  (see also Sect. 3.3 below). This uncertainty affects our absolute estimates of the column densities, densities, and masses of individual sources (Sect. 3.2 and Tables 1 to 3 below), but not our general conclusions of Sects. 4 to 6.

We also assume a volume-averaged dust temperature of  $T_{\text{dust}} = 30$  K for the circumstellar material around  $\rho$  Oph YSOs (cf. AM94), and a uniform dust temperature for dense cores and pre-stellar clumps. Based on AWM93 for  $\rho$  Oph-A and on recent 180–1100  $\mu\text{m}$  dust continuum observations with the balloon-borne PRONAOS/SPM experiment (Ristorcelli et al. 1997) for other parts of  $\rho$  Oph, we adopt dust temperatures ranging from

<sup>1</sup> The strong southern continuum component of Oph-C, centered on ( $\alpha_{1950} = 16^{\text{h}}23^{\text{m}}55^{\text{s}}.5$ ,  $\delta_{1950} = -24^{\circ}26'16''$ ), is here called Oph-C-S.

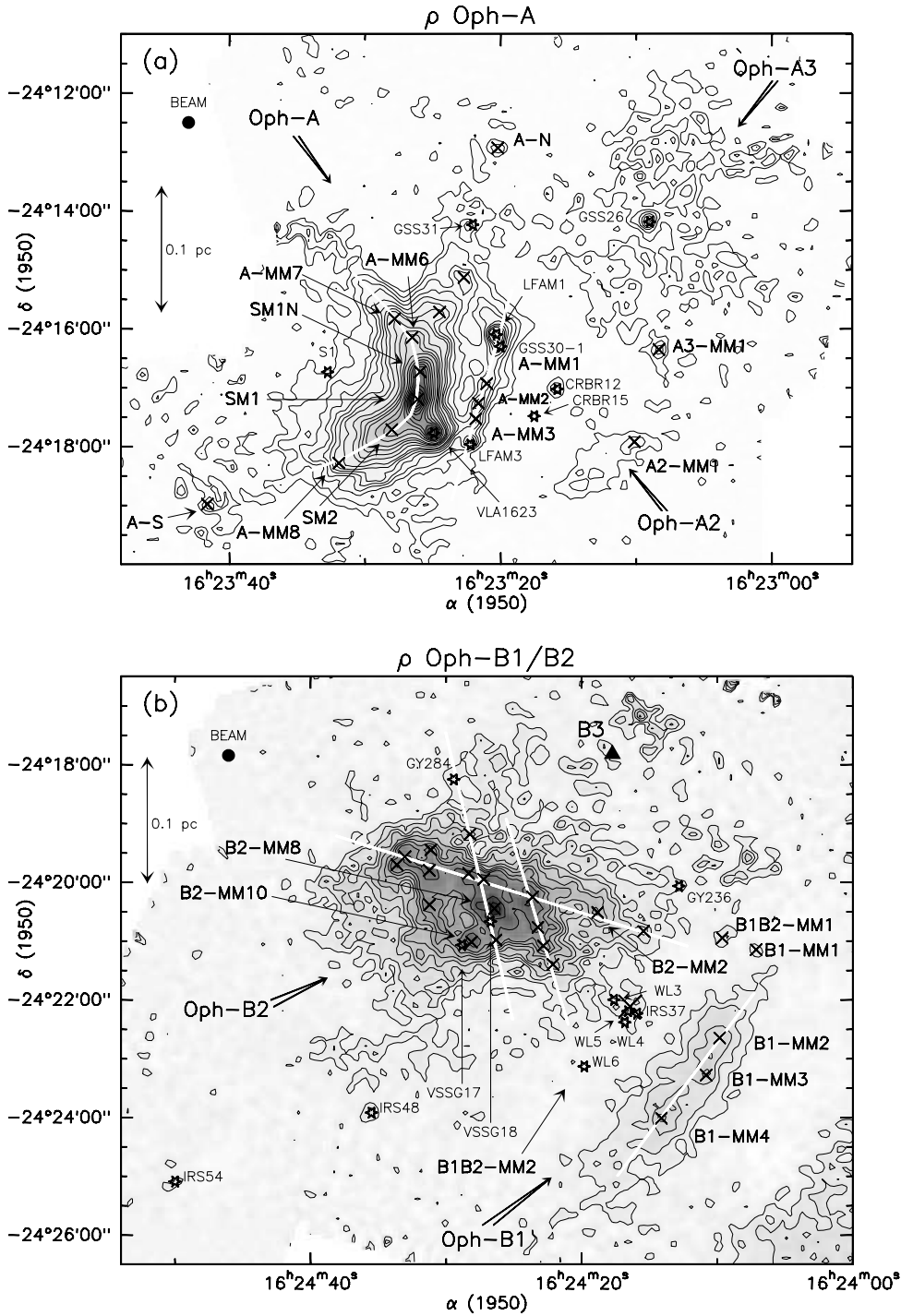


**Fig. 2a–h** Millimeter continuum maps of the DCO<sup>+</sup> dense cores Oph-A, Oph-B1/B2, Oph-C, Oph-D, Oph-E, Oph-F, and of several new, more diffuse cores. These maps are extracted from the mosaic of Fig. 1 and smoothed to an effective angular resolution of 13''. Contour levels go from 25 to 200 mJy/13''-beam with steps of 25 mJy/13''-beam, then from 250 to 400 mJy/13''-beam by 50 mJy/13''-beam and finally from 500 to 1400 mJy/13''-beam by increments of 100 mJy/13''-beam. Starless clumps (Table 2) are denoted by crosses and several young embedded stars (Table 3 and Table 5) by star markers. A few chains of clumps and YSOs are emphasized by white curves. **a** Oph-A and the lower density cores Oph-A2 ( $\alpha_{1950} = 16^{\text{h}}23^{\text{m}}11^{\text{s}}.7$ ,  $\delta_{1950} = -24^{\circ}18'11''$ ), Oph-A3 ( $\alpha_{1950} = 16^{\text{h}}23^{\text{m}}07^{\text{s}}.9$ ,  $\delta_{1950} = -24^{\circ}13'55''$ ); mean rms noise level  $\sim 9$  mJy/13''-beam. **b** Oph-B1 and Oph-B2; mean rms noise level  $\sim 10$  mJy/13''-beam.

12 K to 20 K in the various dense cores (see Table 1). Note that the gas kinetic temperatures estimated by Loren et al. (1980) and Loren (1989) are significantly higher as they are probably

dominated by the warmer, large-scale ambient cloud ( $T \sim 30$  K – e.g., Ristorcelli et al. 1997).

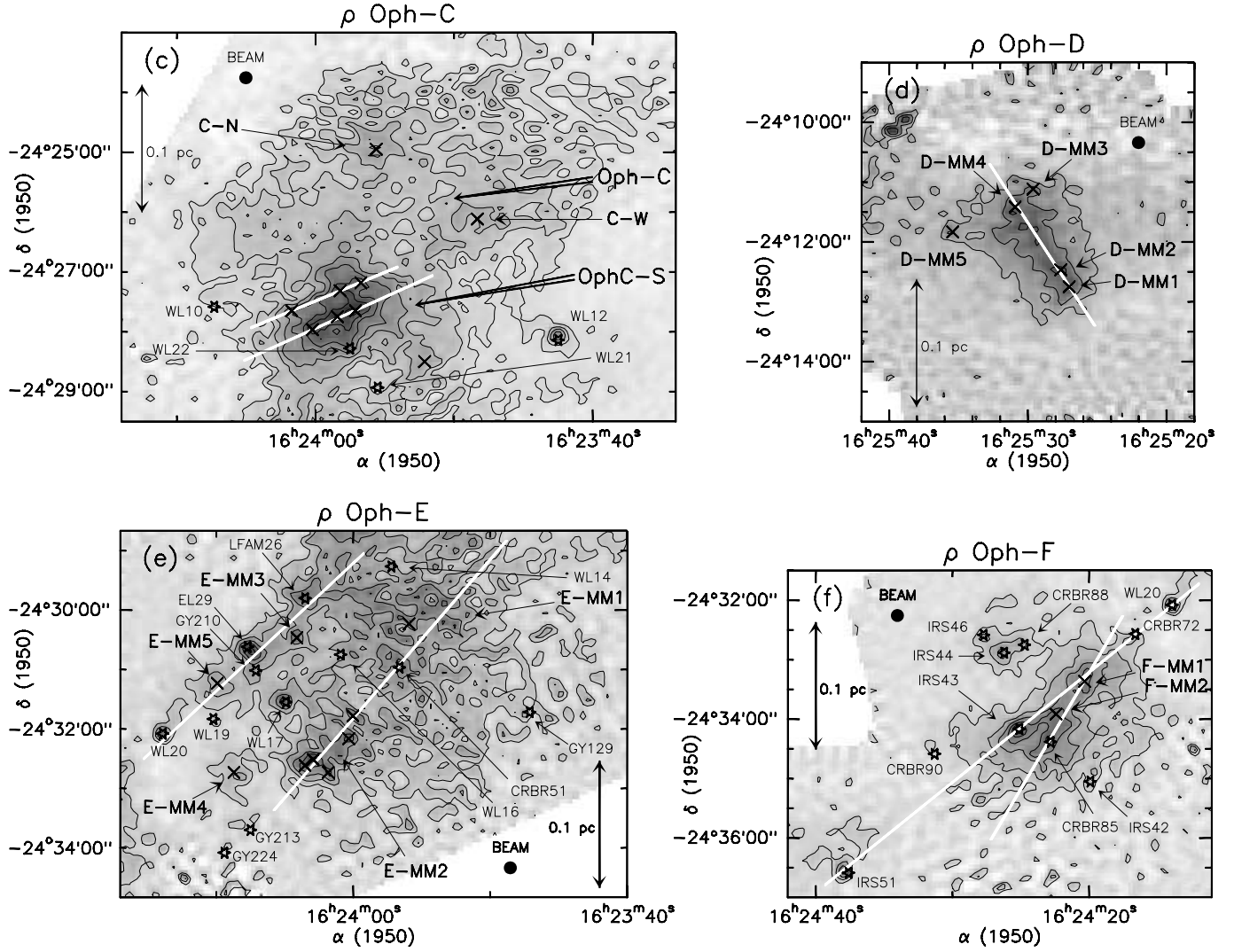


**Fig. 2.** (continued) **c** Oph-C ( $\alpha_{1950} = 16^{\text{h}}23^{\text{m}}55^{\text{s}}.5$ ,  $\delta_{1950} = -24^{\circ}26'16''$ ) and Oph-S ( $\alpha_{1950} = 16^{\text{h}}23^{\text{m}}57^{\text{s}}.9$ ,  $\delta_{1950} = -24^{\circ}27'38''$ ); mean rms noise level  $\sim 5$  mJy/13''-beam. **d** Oph-D ( $\alpha_{1950} = 16^{\text{h}}25^{\text{m}}29^{\text{s}}.6$ ,  $\delta_{1950} = -24^{\circ}12'01''$ ); mean rms noise level  $\sim 5$  mJy/13''-beam. **e** Oph-E; mean rms noise level  $\sim 7$  mJy/13''-beam. **f** Oph-F; mean rms noise level  $\sim 8$  mJy/13''-beam.

### 3.2. Multi-scale structure in the 1.3 mm continuum mosaic

For the purpose of this paper, we have divided the various structures and fragments seen in the 1.3 mm mosaic into ‘cores’ and ‘clumps’, depending on their characteristic lengthscales. We used a multiresolution wavelet analysis<sup>2</sup> (e.g. Starck et al. 1995, see also Langer et al. 1993) to separate 1'-6'-scale structures (i.e., 0.05 pc to 0.3 pc, or 10 000 AU to 60 000 AU), here

<sup>2</sup> Briefly, the wavelet transform of an image  $I_0$  consists in a series of filtering operations which provides “views”  $V_j$  of that image at different spatial scales. The “view”  $V_j$  at scale  $j$  is obtained by convolving the smoothed image at level  $j-1$ ,  $I_{j-1}$ , with the low-pass filter  $H = t(\frac{1}{16}, \frac{1}{4}, \frac{3}{8}, \frac{1}{4}, \frac{1}{16}) \otimes (\frac{1}{16}, \frac{1}{4}, \frac{3}{8}, \frac{1}{4}, \frac{1}{16})$ , and by retaining the difference with the resulting smoothed image at level  $j$ :  $I_j = H * I_{j-1}$ ,  $V_j = I_{j-1} - I_j$ . The original image can be expressed as the sum of all wavelet views (also called planes) plus the smoothed image:  $I_0 = I_p + \sum_j V_j$ . Here, we have considered a total of  $p = 6$  planes with characteristic scales of 16'', 32'', 64'', 128'', 256'', and 512''; the ‘clumps’ are seen in the first two planes and the ‘cores’ in the last four.

called ‘cores’, from smaller 15''-30''-scale (i.e., 2 400 AU to 5 000 AU) ‘clumps’.

The various types of identified structures are discussed in turn below. In practice, there is a good correspondence between the larger 1.3 mm structures and the DCO<sup>+</sup> cores identified by LWW90 (see Sect. 3.2.1 and Table 1). The small-scale ‘clumps’ include both starless cloud fragments (see Sect. 3.2.2 and Table 2) and YSO circumstellar structures (Sect. 3.2.3, Table 3 and Table 5). They do not show any significant substructure at 15'' resolution (except 4 composite clumps in Table 2), while, by contrast, the 1.3 mm continuum emission from ‘cores’ is generally seen to be highly structured. The starless cloud fragments were extracted from the 15''-resolution mosaic in order to improve the signal-to-noise ratio on weak clumps with uncertain peak positions.

The flux and size estimates for starless clumps and YSOs (see Table 2, Table 3, and Table 5) were derived after subtracting the background emission arising from both dense cores and

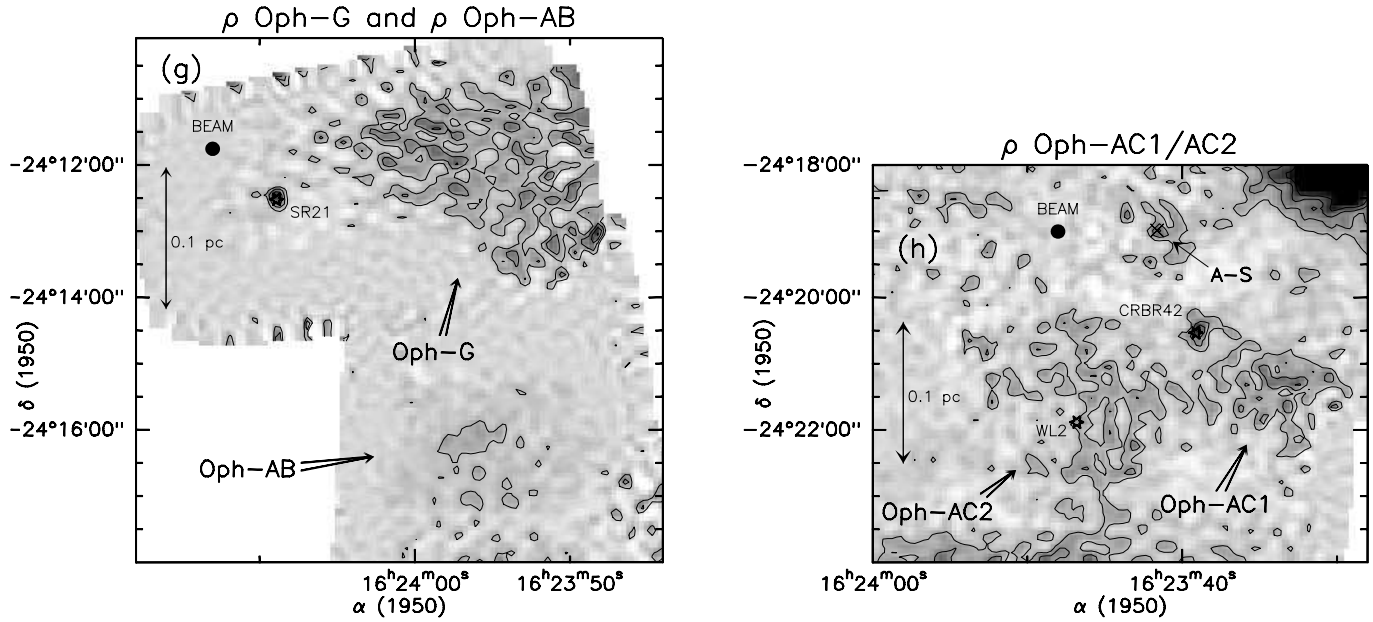


**Fig. 2.** (continued) **g** Oph-G ( $\alpha_{1950} = 16^{\text{h}}23^{\text{m}}54^{\text{s}}.8$ ,  $\delta_{1950} = -24^{\circ}11'58''$ ; incompletely mapped) and Oph-AB ( $\alpha_{1950} = 16^{\text{h}}23^{\text{m}}55^{\text{s}}.8$ ,  $\delta_{1950} = -24^{\circ}16'42''$ ), new diffuse cores; mean rms noise level  $\sim 10$  mJy/13''-beam. **h** Oph-AC1 ( $\alpha_{1950} = 16^{\text{h}}23^{\text{m}}34^{\text{s}}.6$ ,  $\delta_{1950} = -24^{\circ}21'15''$ ) and Oph-AC2 ( $\alpha_{1950} = 16^{\text{h}}23^{\text{m}}45^{\text{s}}.4$ ,  $\delta_{1950} = -24^{\circ}21'51''$ ), new diffuse cores; mean rms noise level  $\sim 15$  mJy/13''-beam. Here, contour levels go from 30 to 120 mJy/13''-beam with steps of 30 mJy/13''-beam.

**Table 1.** Core properties

Core Name (1)	$T_{\text{dust}}$ (K) (2)	FWHM (pc $\times$ pc) (3)	$\langle N_{\text{H}_2} \rangle_{1.3}^{11''}$ ( $10^{22}$ cm $^{-2}$ ) (4)	$\langle n_{\text{H}_2} \rangle_{1.3}^{11''}$ (cm $^{-3}$ ) (5)	$\langle N_{\text{H}_2} \rangle_{1.3}^{1.1'}$ ( $10^{22}$ cm $^{-2}$ ) (6)	$\langle N_{\text{H}_2} \rangle_{\text{C}^{18}\text{O}}^{1.1'}$ ( $10^{22}$ cm $^{-2}$ ) (7)	$M_{1.3}$ ( $M_{\odot}$ ) (8)	$M_{\text{vir}}$ ( $M_{\odot}$ ) (9)	YSO surf. dens. [stars/(0.1 pc) $^2$ ] (10)
Oph-A	20	0.08 $\times$ 0.05	78	$4.0 \times 10^6$	19	6.3-15	23	16-27	2.4-4.4
Oph-A2	20	0.07 $\times$ 0.03	4.3	$3.0 \times 10^5$			0.7		<1.5
Oph-A3	20	0.16 $\times$ 0.08	5.4 – 6.3	$1.5 - 1.8 \times 10^5$			3.9		0.8
Oph-B1	12	0.14 $\times$ 0.05	12	$4.6 \times 10^5$	4.2	3.9-9.2	7.2	24-40	0.45
Oph-B2	12	0.15 $\times$ 0.08	41	$1.2 \times 10^6$	18.4	4.2-10	42	40-66	0.55
OphC-S	12	0.11 $\times$ 0.08	22	$7.6 \times 10^5$	11	3.9-9.8	18	11-19	0.55
Oph-C	12	0.29 $\times$ 0.15	7 – 12	$1.1 - 1.9 \times 10^5$	$\sim 5.1$	-	44	25-42	0.65
Oph-D	12	0.09 $\times$ 0.06	12	$5.3 \times 10^5$	2.1 (in 2')	1.1 (in 2')	5.3	2.8-4.6	<0.6
Oph-E	15	0.22 $\times$ 0.16	8 – 10	$1.4 - 1.7 \times 10^5$	$\sim 3.0$	4.9-12	27	28-47	2.1
Oph-F	15	0.11 $\times$ 0.07	10	$3.7 \times 10^5$	4.3	5.6-13	8.1	16-26	2.9-4.6
Oph-G	20	0.15 $\times$ 0.11	2.8 – 4.3	$0.7 - 1.1 \times 10^5$			4.5		<0.2
Oph-AB	20	0.14 $\times$ 0.10	2.8	$0.8 \times 10^5$			2.3		0.7
Oph-AC1	12	0.12 $\times$ 0.07	10	$3.5 \times 10^5$			3.8		0.4
Oph-AC2	12	0.10 $\times$ 0.05	8.8	$4.0 \times 10^5$			5.1		0.65

Meaning of columns:

- (2) Assumed dust temperature (based on AWB93 and Ristorcelli et al. 1997).
- (3) 2D-Gaussian FWHM measured on 1.3 mm continuum map and deconvolved from beam.
- (4) Peak column density at 1.3 mm in an 11'' beam. A range is given when no clear maximum can be distinguished.
- (5) Peak density at 1.3 mm derived from col. [3] and col. [4]:  $\langle n_{\text{H}_2} \rangle = \langle N_{\text{H}_2} \rangle / \text{FWHM}$ .
- (6) Column density derived from 1.3 mm continuum data averaged over 1.1' C $^{18}$ O beam (2' for Oph-D) centered on peak of each core.
- (7) Column density in 1.1' beam (2' for Oph-D) derived from C $^{18}$ O maps of WL83 and Butner et al. (1995) under LTE hypothesis.
- (8) Gas + dust mass estimated from 1.3 mm continuum map in elliptical area twice the size of col. [3].
- (9) Virial mass assuming a spherical core with  $\rho \propto r^{-2}$  (resp. uniform) density and a diameter twice the size of col. [3]:  $M_{\text{vir}} = 3R\sigma^2/G$  (resp.  $M_{\text{vir}} = 5R\sigma^2/G$ ). Core velocity dispersion  $\sigma$  derived from DCO $^+$  line width measured by LWW90 or Butner et al. (1995).
- (10) Surface number density of mid-IR sources detected by ISOCAM (e.g. Bontemps et al. 1998) within elliptical area twice the size of col. [3], together with estimate within  $3\sigma$  contour level for the compact cores Oph-A and Oph-F.

the large-scale molecular cloud. To do so, a circular area of diameter  $10''$ - $30''$  (resp.  $10''$ - $20''$  for YSOs) believed to contain most of the clump (resp. YSO) emission was first masked, and the surrounding cloud emission was smoothed and interpolated at the clump (resp. YSO) position. The estimated background emission was then subtracted from the original mosaic to produce a map of the target's intrinsic emission. The uncertainties associated with this procedure depend on the complexity of the local background/environment and are listed along with the extracted fluxes in Table 2, Table 3, and Table 5. Note that the clump coordinates given in Table 2 are only accurate to  $5''$ - $10''$ .

### 3.2.1. Cores

The main characteristics of the  $1'$ - $6'$  'cores' as derived from our 1.3 mm continuum data are listed in Table 1. These cores can be tentatively divided into three groups. First, Oph-A, Oph-B1, Oph-B2, OphC-S, Oph-D, and Oph-F correspond to  $\text{DCO}^+$  cores that are highly 'centrally condensed' (see Figs. 2a, 2b, 2c, 2d, 2f). These are relatively compact with FWHM sizes  $\lesssim 0.1$  pc ( $\sim 2'$ ), and have peak densities in the range  $n_{\text{H}_2} \sim 4\text{--}40 \times 10^5 \text{ cm}^{-3}$  (and peak column densities  $N_{\text{H}_2} \sim 10\text{--}80 \times 10^{22} \text{ cm}^{-2}$ ).

Second, the  $\text{DCO}^+$  cores Oph-C and Oph-E are morphologically different from the previous cores: they consist of broader ( $\sim 4'$ ), clumpy emission 'plateaux' with  $n_{\text{H}_2} \sim 1.5 \times 10^5 \text{ cm}^{-3}$  (and  $N_{\text{H}_2} \sim 9 \times 10^{22} \text{ cm}^{-2}$ ), which are clearly not centrally condensed (see Figs. 2c, 2e).

The third type of cores comprises a number of weaker ( $< N_{\text{H}_2} > \sim 5 \times 10^{22} \text{ cm}^{-2}$ ) structures identified in the mosaic of Fig. 1 (see Figs. 2a, 2g, and 2h), but undetected by LW90 in  $\text{DCO}^+$ . The structure of these 'diffuse cores' is apparently clumpy, but is more uncertain than that of the stronger  $\text{DCO}^+$  cores.

### 3.2.2. Starless clumps

The characteristics of the  $15''$ - $30''$  starless 'clumps' identified in our 1.3 mm continuum maps (Figs. 2a-2h) are listed in Table 2. Here, 'starless' means absence of near-IR, mid-IR, and radio continuum sources, from ground-based IR surveys (e.g. Barsony et al. 1997), ISOCAM surveys (e.g. Nordh et al. 1996, Bontemps et al. 1998), and VLA surveys (e.g. LFAM), respectively.

We are reasonably confident of the existence of most of these clumps because they consistently appear in independent bolometer coverages. In all cases, the contrast with respect to the local 'environment' in the  $15''$ -resolution mosaic is at the  $5\sigma$  level at least. Furthermore, many clumps of Table 2 are associated with deep *absorption* features in the ISOCAM  $6.75 \mu\text{m}/15 \mu\text{m}$  images of Abergel et al. (1996). These 'negative' ISOCAM features are interpreted as dense cores seen in absorption against the diffuse mid-IR background arising from the cloud envelope (see Abergel et al. 1997 and Bacmann et al. 1998).

Our list of identified 1.3 mm clumps is in good agreement with the extraction of cloud fragments carried out by Pound & Blitz (1995) on their lower ( $30''$ ) resolution  $800 \mu\text{m}$  and  $\text{DCO}^+$  maps of Oph-B1 and Oph-B2 (see last column of Table 2).

### 3.2.3. YSO circumstellar structures

Table 3 lists the millimeter counterparts of (Class I and Class II) YSOs which were not observed by AM94. Revised estimates for the 1.3 mm flux densities of the YSOs surveyed by AM94 are given in Appendix A (Table 5).

Since the  $\rho$  Oph cores are highly structured, the probability of chance coincidence between a near-IR source and an unrelated clump such as those of Table 2 must be considered. For any given detected YSO from Table 3 and Table 5, the probability to find a 1.3 mm emission peak greater than the  $5\sigma$  level within a  $10''$  diameter circle around the nominal YSO position is  $\sim 0.3\%$ . This probability is slightly higher for a source lying over a core ( $0.6\%$ ) and/or detected at a weaker level. Altogether, among the 31 YSOs detected above  $5\sigma$  in Table 3 and Table 5, the expected number of misidentified sources is only  $\sim 0.09\text{--}0.2$ . The 1.3 mm fluxes of ten sources in Table 3 and Table 5 are less secure (and given in parentheses) as the associated emission peaks are only at the  $3\sigma$  or  $4\sigma$  level. The last four detections of Table 3 are only tentative since the 1.3 mm peaks are  $5''$ - $10''$  away from the nominal near-IR positions, and the corresponding number of chance coincidences is  $\sim 1.3$ . We interpret the millimeter continuum peaks observed  $\sim 10''\text{--}15''$  away from GY 10, GY 11, VSSG 17, and VSSG 18 (see Figs. 2a, 2b) as arising from cloud structure rather than circumstellar emission.

It is noteworthy that the Class I YSOs tend to be found in the inner parts of the dense cores, while the Class II sources lie preferentially on the outskirts of the cores. For instance, the mean projected distance from core center is  $\sim 13\,000$  AU (i.e.,  $1.4'$ ) for Class I/flat-spectrum sources in Oph-A and Oph-F, while it is  $\sim 25\,000$  AU (i.e.,  $2.6'$ ) for Class II sources. There are also several relatively isolated Class I objects, such as IRS 51 and WL 12, which are not associated with any particular dense core but lie over a low-density 'diffuse' medium.

### 3.3. Comparison with molecular line maps

Molecular maps in optically thin  $\text{C}^{18}\text{O}$  lines, which trace the spatial distribution of the gas column density, should in principle be directly comparable to our dust continuum results (cf. Schwartz, Snell, & Schloerb 1989). Maps in dense molecular tracers such as  $\text{DCO}^+$  are sensitive to the spatial distribution of the cold, high-density (e.g.,  $n_{\text{crit}} \sim 5.1 \times 10^5 \text{ cm}^{-3}$  for  $\text{DCO}^+(2\text{--}1)$  – cf. Butner et al. 1995) gas and may more accurately reflect the structure of dense cores.

Our 1.3 mm estimates for the column densities and masses of the  $\text{DCO}^+$  cores<sup>3</sup> are compared in Table 1 with estimates derived

<sup>3</sup> We here consider the list of  $\text{DCO}^+$  cores by LW90. However, we do not take their Oph-B3 position as an independent dense core since only little 1.3 mm continuum emission is associated with it (see triangular marker in Fig. 2b). Furthermore, the nominal  $\text{DCO}^+$  position they give for Oph-C is  $3'$  NW from the compact dense core we call OphC-S (see Fig. 2c). This core coincides with a  $\text{C}^{18}\text{O}$  peak (see Fig. 3a) but was apparently not detected in  $\text{DCO}^+$  by LW90 (see Fig. 3b). Oph-C itself corresponds to a broad plateau of 1.3 mm continuum emission (see Fig. 2c).

**Table 2.** Characteristics of ‘starless’ clumps detected at 1.3 mm

Source Name	Coordinates		$S_{1.3mm}^{peak}$ <sup>(1)</sup> (mJy/beam)	FWHM <sup>(2)</sup> (AU $\times$ AU)	M <sup>(3)</sup> ( $M_{\odot}$ )	$M_{BE}^{(4)}$ ( $M_{\odot}$ )	$n_{H_2}$ <sup>(5)</sup> ( $cm^{-3}$ )	CAM abs. <sup>(6)</sup>	Comments and references <sup>(7)</sup>
	$\alpha_{1950}$ 16 <sup>h</sup>	$\delta_{1950}$ -24 <sup>o</sup>							
A3-MM1	23 <sup>m</sup> :08 <sup>s</sup> .3	16 <sup>′</sup> :21 <sup>″</sup>	90 $\pm$ 10	unresolved	0.10	0.08	$6.6 \times 10^7$	N	compact, protostellar ?
A2-MM1	23:09.9	17:55	60 $\pm$ 10	4500 $\times$ 960	0.10	0.20	$4.0 \times 10^6$	N	diffuse, pre-collapse ?
A-N	23:20.2	12:56	60 $\pm$ 10	unresolved	0.06	0.08	$3.8 \times 10^7$	N	compact, protostellar ?
A-MM1	23:21.0	16:56	50 $\pm$ 15	unresolved	0.05	0.08	$3.1 \times 10^7$	N	rel. to VLA 1623 outflow ?
A-MM2	23:21.6	17:16	90 $\pm$ 15	unresolved	0.08	0.08	$5.7 \times 10^7$	N	rel. to VLA 1623 outflow ?
A-MM3	23:21.8	17:32	55 $\pm$ 15	unresolved	0.05	0.08	$3.5 \times 10^7$	N	rel. to VLA 1623 outflow ?
A-MM4	23:22.7	15:08	80 $\pm$ 15	4000 $\times$ 1400	0.14	0.23	$3.5 \times 10^6$	N	diffuse, pre-collapse ?
A-MM5	23:24.5	15:43	100 $\pm$ 20	3700 $\times$ 2900	0.23	0.32	$2.3 \times 10^6$	N	diffuse, pre-collapse ?
SM1N	23:25.9	16:44	790 $\pm$ 25	3000 $\times$ 1800	1.3	0.22	$3.6 \times 10^7$	N	compact, protostellar ? ; rel. to S1 PDR ? ; AWB93
SM1	23:26.1	17:12	1300 $\pm$ 20	6100 $\times$ 2100	3.2	0.34	$2.4 \times 10^7$	N	compact, protostellar ? ; rel. to S1 PDR ? ; AWB93
A-MM6	23:26.5	16:09	200 $\pm$ 25	3200 $\times$ 2700	0.4	0.28	$5.3 \times 10^6$	N	diffuse, pre-collapse ? ; rel. to S1 PDR ? ; Mezger92b (FIR1)
A-MM7	23:27.8	15:50	110 $\pm$ 30	1400 $\times$ 1400	0.13	0.13	$1.5 \times 10^7$	N	rel. to S1 PDR ?
SM2	23:28.0	17:43	450 $\pm$ 30	6200 $\times$ 3400	1.3	0.44	$4.7 \times 10^6$	N	diffuse, pre-collapse ? ; rel. to S1 PDR ? ; AWB93
A-MM8	23:31.9	18:17	80 $\pm$ 25	2900 $\times$ 2100	0.13	0.24	$3.1 \times 10^6$	N	rel. to S1 PDR ?
A-S	23:41.6	18:59	85 $\pm$ 10	unresolved	0.08	0.08	$5.4 \times 10^7$	Y+	compact, protostellar ?
B1-MM1	24:07.1	21:09	50 $\pm$ 5	unresolved	0.10	0.05	$6.5 \times 10^7$	Y	compact, protostellar ? ; PB95 (DCO <sup>+</sup> 8)
B1-MM2	24:09.7	22:37	45 $\pm$ 10	3000 $\times$ 2100	0.17	0.14	$3.8 \times 10^6$	Y+	PB95 (20 <sup>″</sup> from DCO <sup>+</sup> 9 & 10)
B1-MM3	24:10.8	23:17	65 $\pm$ 10	1800 $\times$ 1300	0.16	0.09	$1.7 \times 10^7$	Y	PB95 (C2, 10 <sup>″</sup> from DCO <sup>+</sup> 13)
B1-MM4	24:14.1	24:01	60 $\pm$ 15	4600 $\times$ 3200	0.21	0.22	$1.3 \times 10^6$	Y+	diffuse, pre-collapse ? ; PB95 (30 <sup>″</sup> from DCO <sup>+</sup> 4)
B1B2-MM1	24 <sup>m</sup> :09 <sup>s</sup> .7	20 <sup>′</sup> :58 <sup>″</sup>	40 $\pm$ 5	2700 $\times$ 1800	0.10	0.13	$3.2 \times 10^6$	N	PB95 (20 <sup>″</sup> from C4 & DCO <sup>+</sup> 7)
B1B2-MM2	24:16.4	22:07	45 $\pm$ 10	4800 $\times$ 4100	0.33	0.26	$1.3 \times 10^6$	N	composite pre-collapse clump
B2-MM1	24:15.4	20:51	60 $\pm$ 10	$\sim$ unresolved	0.14	0.05	$9.1 \times 10^7$	Y+	
B2-MM2	24:18.7	20:28	85 $\pm$ 10	4500 $\times$ 2400	0.47	0.19	$4.5 \times 10^6$	Y+	PB95 (15 <sup>″</sup> from DCO <sup>+</sup> 3)
B2-MM3	24:22.1	21:25	60 $\pm$ 10	unresolved	0.12	0.05	$7.8 \times 10^7$	Y	
B2-MM4	24:22.7	21:05	90 $\pm$ 15	2100 $\times$ 960	0.27	0.08	$3.3 \times 10^7$	Y	compact, protostellar ?
B2-MM5	24:23.3	20:46	100 $\pm$ 15	2200 $\times$ 960	0.26	0.08	$2.9 \times 10^7$	Y+	
B2-MM6	24:23.7	20:20	150 $\pm$ 15	4300 $\times$ 2700	0.78	0.20	$6.6 \times 10^6$	Y	
B2-MM7	24:26.3	20:59	100 $\pm$ 20	$\sim$ unresolved	0.23	0.05	$1.6 \times 10^8$	Y	
B2-MM8	24:26.4	20:27	215 $\pm$ 20	4000 $\times$ 4000	1.5	0.23	$7.8 \times 10^6$	Y	diffuse, pre-collapse ? ; PB95 (C1, 35 <sup>″</sup> from DCO <sup>+</sup> 1)
B2-MM9	24:27.2	19:57	110 $\pm$ 15	1600 $\times$ 960	0.31	0.07	$5.6 \times 10^7$	Y	
B2-MM10	24:28.0	21:02	160 $\pm$ 10	3400 $\times$ 2200	0.6	0.16	$9.7 \times 10^6$	Y	compact, protostellar ?
B2-MM11	24:28.3	19:09	75 $\pm$ 15	unresolved	0.15	0.05	$9.8 \times 10^7$	Y	
B2-MM12	24:28.3	19:53	140 $\pm$ 10	2100 $\times$ 1300	0.39	0.10	$3.1 \times 10^7$	Y	
B2-MM13	24:31.1	19:27	75 $\pm$ 15	$\sim$ unresolved	0.19	0.05	$1.3 \times 10^8$	Y	
B2-MM14	24:31.2	19:49	130 $\pm$ 15	2100 $\times$ 1800	0.43	0.11	$2.1 \times 10^7$	Y+	
B2-MM15	24:31.2	20:23	90 $\pm$ 15	unresolved	0.17	0.05	$1.2 \times 10^8$	Y	compact, protostellar ?
B2-MM16	24:32.9	19:33	100 $\pm$ 15	2700 $\times$ 1300	0.35	0.11	$1.8 \times 10^7$	Y	
B2-MM17	24:33.6	19:42	90 $\pm$ 15	$\sim$ unresolved	0.23	0.05	$1.6 \times 10^8$	Y+	
C-W	23:48.3	26:07	50 $\pm$ 10	17000 $\times$ 8000	1.4	0.67	$3.0 \times 10^5$	Y	composite pre-collapse clump
C-MM1	23:52.0	28:29	50 $\pm$ 10	5900 $\times$ 3000	0.35	0.24	$1.6 \times 10^6$	Y	diffuse, pre-collapse ?
C-N	23:55.6	24:57	60 $\pm$ 10	10000 $\times$ 8800	1.7	0.54	$7.3 \times 10^5$	Y	composite pre-collapse clump ?
C-MM2	23:56.7	27:11	45 $\pm$ 10	$\sim$ unresolved	0.12	0.05	$1.2 \times 10^7$	Y	
C-MM3	23:57.2	27:40	55 $\pm$ 25	5400 $\times$ 640	0.23	0.11	$6.5 \times 10^7$	Y	
C-MM4	23:57.7	27:20	50 $\pm$ 15	2400 $\times$ 1400	0.16	0.11	$2.0 \times 10^6$	Y	
C-MM5	23:58.4	27:45	50 $\pm$ 25	unresolved	0.10	0.05	$7.8 \times 10^7$	Y	
C-MM6	23:59.9	27:55	60 $\pm$ 20	4000 $\times$ 3700	0.33	0.22	$8.3 \times 10^6$	Y	
C-MM7	24:01.6	27:40	50 $\pm$ 15	$\sim$ unresolved	0.13	0.05	$8.5 \times 10^7$	Y	

**Table 2.** (continued) Characteristics of ‘starless’ clumps detected at 1.3 mm

Source Name	Coordinates		$S_{1.3mm}^{peak}$ <sup>(1)</sup> (mJy/beam)	FWHM <sup>(2)</sup> (AU $\times$ AU)	M <sup>(3)</sup> ( $M_{\odot}$ )	$M_{BE}^{(4)}$ ( $M_{\odot}$ )	$n_{H_2}$ <sup>(5)</sup> ( $cm^{-3}$ )	CAM abs. <sup>(6)</sup>	Comments and references <sup>(7)</sup>
	$\alpha_{1950}$ 16 <sup>h</sup>	$\delta_{1950}$ –24 <sup>o</sup>							
D-MM1	25:27.0	12:45	45 $\pm$ 5	2700 $\times$ 1700	0.15	0.12	5.1 $\times$ 10 <sup>6</sup>	Y	
D-MM2	25:27.6	12:28	45 $\pm$ 15	4000 $\times$ 2600	0.16	0.19	1.6 $\times$ 10 <sup>6</sup>	Y	diffuse, pre-collapse ?
D-MM3	25:29.6	11:07	30 $\pm$ 5	~unresolved	0.08	0.05	5.2 $\times$ 10 <sup>7</sup>	Y	
D-MM4	25:30.9	11:25	40 $\pm$ 10	3800 $\times$ 2600	0.17	0.18	1.9 $\times$ 10 <sup>6</sup>	Y+	diffuse, pre-collapse ?
D-MM5	25:35.4	11:50	35 $\pm$ 5	unresolved	0.07	0.05	4.6 $\times$ 10 <sup>7</sup>	N	
E-MM1	23:55.9	30:14	55 $\pm$ 20	23000 $\times$ 19000	2.2	1.2	8.1 $\times$ 10 <sup>4</sup>	Y	composite pre-collapse clump
E-MM2a	24:59.8	31:47	50 $\pm$ 15	unresolved	0.07	0.06	4.7 $\times$ 10 <sup>7</sup>	N	
E-MM2b	24:00.3	32:10	60 $\pm$ 15	unresolved	0.08	0.06	5.6 $\times$ 10 <sup>7</sup>	Y	
E-MM2c	24:01.8	32:44	60 $\pm$ 15	unresolved	0.08	0.06	5.6 $\times$ 10 <sup>7</sup>	Y	
E-MM2d	24:03.1	32:34	110 $\pm$ 20	4200 $\times$ 2700	0.45	0.24	4.0 $\times$ 10 <sup>5</sup>	Y	diffuse, pre-collapse ?
E-MM3	24:04.1	30:28	60 $\pm$ 10	unresolved	0.08	0.06	5.6 $\times$ 10 <sup>7</sup>	Y	compact, protostellar ?
E-MM4	24:08.8	32:49	50 $\pm$ 10	6900 $\times$ 5300	0.44	0.44	6.9 $\times$ 10 <sup>5</sup>	Y+	diffuse, pre-collapse ?
E-MM5	24:10.0	31:16	55 $\pm$ 10	7700 $\times$ 4600	0.42	0.43	6.8 $\times$ 10 <sup>5</sup>	Y+	diffuse, pre-collapse ?
F-MM1	24:20.2	33:19	65 $\pm$ 20	4800 $\times$ 2600	0.25	0.26	2.0 $\times$ 10 <sup>6</sup>	Y	diffuse, pre-collapse ?
F-MM2	24:22.4	33:55	50 $\pm$ 15	2700 $\times$ 1600	0.12	0.15	4.5 $\times$ 10 <sup>6</sup>	Y	diffuse, pre-collapse ?

Notes:

- (1) Peak flux in 15''-beam estimated after background subtraction. Uncertainty mainly due to environment subtraction but also including map rms measured at source position.
- (2) Deconvolved FWHM derived from 2D-Gaussian fit after background subtraction.
- (3) Mass derived from flux integration (after background subtraction) over area twice the size of col. [5] in 15''-resolution map. A smaller integration area was used when other features (YSOs and/or clumps) are present.  $T_{dust}$  taken from Table 1; dust opacity assumed to be  $\kappa_{1.3mm} = 0.005 \text{ cm}^2 \text{ g}^{-1}$ .
- (4) Bonnor-Ebert critical mass,  $M_{BE} = 2.4 Ra_s^2/G$ , derived from the size of col. [5] and the parent core temperature listed in Table 1. An upper limit FWHM of 800 AU was assumed for unresolved clumps.
- (5) Mean density derived from col. [5] and col. [6]:  $\langle n_{H_2} \rangle = M / [\frac{4}{3}\pi \times (FWHM/2)^3]$ . An upper limit FWHM of 800 AU was assumed for unresolved clumps.
- (6) ‘Y’ means clump lies over large-scale ISOCAM 6.75  $\mu\text{m}/15 \mu\text{m}$  absorption feature (e.g. Abergel et al. 1996). ‘Y+’ means the clump itself is seen as a small-scale absorption structure by ISOCAM.
- (7) Centrally condensed ‘compact’ clumps are candidate ‘isothermal protostars’, while ‘diffuse’ clumps with flat inner density profiles are probably ‘pre-collapse’ in nature (see Sect. 5.1).

References for clump cross-identification: Mezger et al. 1992b (Mezger92b), André et al. 1993 (AWB93), Pound &amp; Blitz 1995 (PB95).

from previously published C<sup>18</sup>O and DCO<sup>+</sup> line data (WL83, LWW90, and Butner et al. 1995). A smoothed version of our 1.3 mm mosaic is displayed in Fig. 3a and Fig. 3b, for comparison with the C<sup>18</sup>O(1–0) map of WL83 and the DCO<sup>+</sup>(2–1) map of LWW90 (shown as bold dashed and bold dotted contours, respectively).

The overall continuum morphology is very similar to the C<sup>18</sup>O morphology. Furthermore, it is noteworthy that the main 1.3 mm emission features occur precisely in those areas which have both strong DCO<sup>+</sup> and strong C<sup>18</sup>O emission. This suggests that a high density and a high column density are both required to produce strong dust millimeter continuum emission. We also note that the contrast between the dense cores and the ambient cloud is higher in the continuum maps than in the C<sup>18</sup>O map. The 1.3 mm map recovers most of the dust counterpart of the C<sup>18</sup>O emission, except the faintest large-scale C<sup>18</sup>O features which

remain undetected. The C<sup>18</sup>O emission plateau at  $\langle N_{H_2} \rangle \sim 2-3 \times 10^{22} \text{ cm}^{-2}$  over which the dense cores generally lie is indeed filtered out by the dual-beam technique (see Appendix B).

The column densities derived from our dust continuum maps agree within a factor  $\sim 2-3$  with published C<sup>18</sup>O estimates (cf. Table 1 and Appendix B). Furthermore, our 1.3 mm continuum estimates of the core masses agree to within a factor of 2.5 with the virial mass estimates of LWW90 and Butner et al. (1995), except in the case of Oph-B1 (see Table 1). This is probably due to the fact that Oph-B1 is gravitationally unbound and far from virial equilibrium with  $M_{vir} \sim 5 \times M_{1.3mm}$  (see also LWW90).

In conclusion, our 1.3 mm dust continuum maps appear to probe all of the DCO<sup>+</sup> cores as well as part of the large-scale C<sup>18</sup>O ‘envelopes’. Furthermore, we believe that our column density and mass estimates for the various DCO<sup>+</sup> dense cores are generally accurate to within a factor of  $\gtrsim 2$ .

**Table 3.** New 1.3 mm detections of YSOs

Source Name <sup>(1)</sup>	Coordinates		$S_{1.3\text{mm}}^{\text{peak}}$ <sup>(2)</sup> (mJy/11''-beam)	$S_{30''}^{\text{int}}$ <sup>(3)</sup> (mJy)	$M_{c*}$ <sup>(4)</sup> ( $M_{\odot}$ )	Class and references <sup>(5)</sup>
	$\alpha_{1950}$	$\delta_{1950}$				
CRBR 12	16 <sup>h</sup> :23 <sup>m</sup> :15 <sup>s</sup> .8	-24 <sup>o</sup> :17':00''	85 ± 5	85	0.01	New YSO candidate, Class II ?
CRBR 15	16:23:17.5	-24:17:29	40 ± 5	40	0.006	New YSO candidate, Class II ?
CRBR 42/GY 91	16:23:39.1	-24:20:32	120 ± 15	300	0.085	CRBR Class I candidate
GY 129/WL 18	16:23:47.1	-24:31:43	45 ± 10	85	0.01	Class II (GWAYL)
CRBR 51	16:23:56.6	-24:30:58	35 ± 15	70	0.02	New YSO candidate, Class I ?
LFAM 26	16:24:03.5	-24:29:48.1	75 ± 10	100	0.03	Class I (GWAYL)
GY 210	16:24:07.1	-24:31:01	25 ± 15	40	0.006-0.01	New YSO candidate
GY 236	16:24:13.0	-24:20:04	(35 ± 20)	105	0.03	New YSO candidate, Class I ?
CRBR 85	16:24:22.8	-24:34:23	40 ± 10	150	0.04	CRBR Class I candidate
CRBR 88/GY 262	16:24:24.7	-24:32:42	60 ± 5	60	0.008	Class II (GWAYL)
GY 284	16:24:29.4	-24:18:15	(25 ± 10)	130	0.037	New YSO candidate, Class I ?
GY 213	16:24:07.5	-24:33:42	(?30 ± 10)	40	0.006-0.01	New YSO candidate
GY 224/IRAS 43	16:24:09.4	-24:34:05	(?30 ± 10)	50	0.014	flat spectrum (GWAYL)
CRBR 72/GY 245	16:24:16.6	-24:32:34	?55 ± 5	60	0.017	flat spectrum (CRBR), Class I (GWAYL)
CRBR 90/GY 292	16:24:31.3	-24:34:35	?30 ± 5	30	0.004	Class II (GWAYL)

Notes:

- (1) Source name includes YSO reference: CRBR = Comerón et al. 1993; GY = Greene & Young 1992; LFAM = Leous et al. 1991.
- (2) Peak circumstellar flux in 11'' beam estimated after background subtraction. Uncertainty mainly due to environment subtraction but also including map rms measured at source position. Weak ( $< 5\sigma$ ) detections are given within parentheses. Values preceded by question marks correspond to tentative detections 5'' – 10'' away from nominal position.
- (3) Integrated flux in 30'' diameter area after background subtraction.
- (4) Circumstellar mass deduced from col. [3] using  $\kappa_{1.3\text{mm}} = 0.01 \text{ cm}^2 \text{ g}^{-1}$  for Class I and  $\kappa_{1.3\text{mm}} = 0.02 \text{ cm}^2 \text{ g}^{-1}$  for Class II sources (e.g. AM94). A dust temperature of  $T_{\text{dust}} = 30 \text{ K}$  was assumed.
- (5) All sources have clear ISOCAM counterparts (with “red” colors, i.e., spectral index  $\alpha_{7\mu\text{m}-15\mu\text{m}} > -1.5$ , Bontemps et al. 1998) except GY 210, probably due to confusion by the very bright source EL 29. Sources CRBR 51, GY 236, GY 284 are proposed as new Class I candidates based on their extended 1.3 mm emission ( $S^{\text{int}}/S^{\text{peak}} \gtrsim 3$ ).  
References: CRBR = Comerón et al. 1993; GWAYL = Greene et al. 1994.

### 3.4. Comparison with other dust continuum studies

There is also good agreement between our bolometer-array images and the lower sensitivity 1.3 mm maps of Mezger et al. (1992b) and AWB93. Quite remarkably, we confirm the existence of *all* the clumps that could be tentatively identified in the Mezger et al. maps of Oph-B1, Oph-B2, and Oph-F (i.e., OphB1-MM2 & 3, OphB2-MM8, 9, 10 & 12 and OphF-MM1). In addition, we detect a large number of *new* clumps, which emphasizes the fact that the  $\rho$  Oph cores are highly structured. The mass estimates of Mezger et al. (revised according to our adopted dust temperatures) are consistent with ours to better than 50% for all the cores but Oph-F. Their mass estimate is significantly lower than ours for Oph-F ( $M = 1 M_{\odot}$  vs.  $M = 8.1 M_{\odot}$ ), which is entirely due to the fact that their map of this core is incomplete. In  $\rho$  Oph-A, our bolometer-array map (Fig. 2a) reveals a new filamentary structure located 1' west of core center, in addition to the prominent 1.3 mm continuum clumps called SM1, VLA1623, SM2, and SM1N by AWB93 (see their Fig. 1). The new filament includes several YSOs (LFAM 1, GSS 30, LFAM 3) and starless clumps (labeled OphA-MM1–3 here).

We have also compared our present results with the 1.3 mm YSO fluxes of AM94, which were mostly obtained in the ON-

OFF mode with a 30'' wobbler throw. While this observing mode is insensitive to dust emission more extended than the wobbler throw, the on-the-fly mapping mode used in the present study allows us to partly restore the extended emission. The circumstellar fluxes we derive here are consistent with those published by AM94 (see Table 5 in Appendix A). In particular, we confirm, using another observing method (on-the-fly instead of ON-OFF), the conclusion of AM94 that there is little circumstellar dust around the near-IR sources WL 16, WL 22, and IRS 37, which were originally believed to be young Class I protostars (cf. Adams, Lada, & Shu 1987, WLY). In reality, these three sources are probably highly-obscured YSOs located behind relatively dense extended cores or clumps. In projection onto the sky, WL 16 lies within the large emission plateau corresponding to Oph-E in our map, WL 22 is close to the peak of the prominent OphC-S core, and IRS 37 lies over the starless, composite clump OphB1B2-MM2. We suggest that Oph-E, OphC-S, and OphB1B2-MM2 may be sources of substantial diffuse 60  $\mu\text{m}$  and 100  $\mu\text{m}$  emission, which would account for the classification of WL 16, WL 22, and IRS 37 as Class I sources based on low angular resolution IRAS data (WLY). Recent infrared results support the idea that WL 16 and WL 22 are massive or intermediate-mass Class II objects (e.g. Comerón et al. 1993

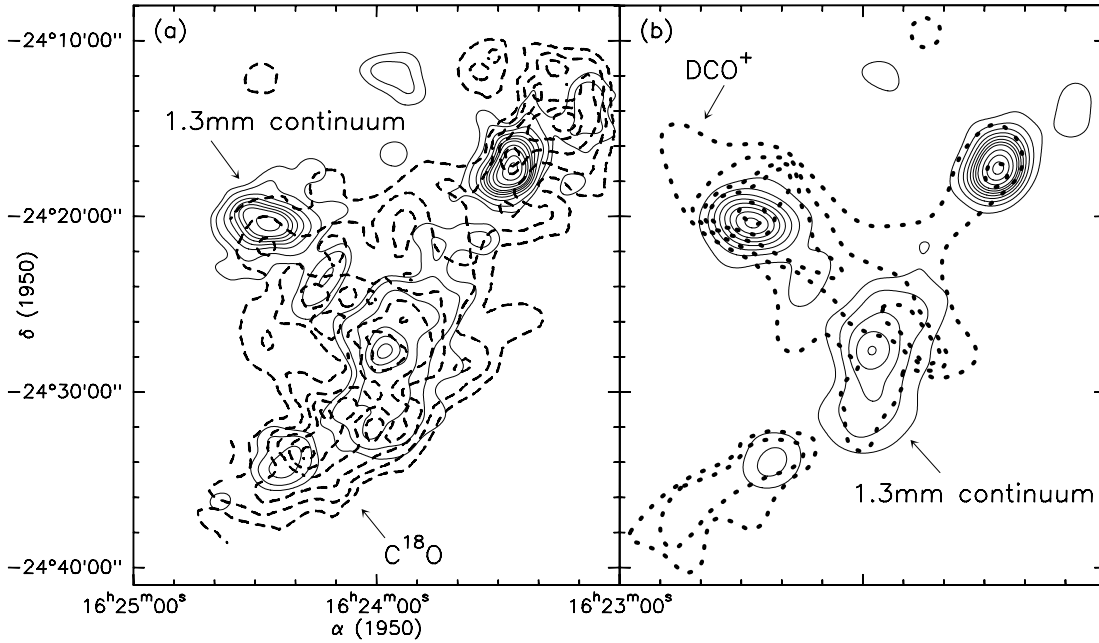


**Fig. 3a and b**  $C^{18}O(1-0)$  map of WL83 (bold dashed contours in **a**) and  $DCO^+(2-1)$  map of LW90 (bold dotted contours in **b**) superposed on our millimeter dust continuum map of the  $\rho$  Oph main cloud (solid contours). The continuum data were smoothed to the resolutions of the  $C^{18}O$  and  $DCO^+$  maps, i.e.,  $1.1'$  in **a** and  $1.8'$  in **b**. **a** Solid contours are 0.25 Jy/ $1.1'$ -beam, 0.5 to 3 by steps of 0.5 Jy/ $1.1'$ -beam, and 4, 5, 7, 9 Jy/ $1.1'$ -beam. The dashed contours of the  $C^{18}O(1-0)$  integrated line intensity vary from 3 to 8  $K.km^{-1}.s^{-1}$  by increments of 1  $K.km^{-1}.s^{-1}$ . **b** Solid contours range from 1 to 7 Jy/ $1.8'$ -beam by steps of 1 Jy/beam and from 8 to 14 Jy/ $1.8'$ -beam by 2 Jy/beam. The dotted contours of the  $DCO^+(2-1)$  peak line intensity ( $T_A^*$ ) go from 0.4 K to 2 K by steps of 0.4 K.

– hereafter CRBR, Emerson 1996). ISOCAM detects extended mid-IR halos around both sources (e.g. Bontemps et al. 1998), very likely due to PAH-like emission (see Emerson et al. 1996).

#### 4. Radial structure analysis

As demonstrated by recent studies, sensitive (sub)millimeter continuum observations such as those presented here are a powerful tool to constrain the radial density structure of protostellar envelopes and pre-collapse dense cores. In general, protostellar envelopes in regions of ‘isolated’ star formation such as Taurus have estimated density gradients which range from  $\rho(r) \propto r^{-1.5}$  to  $\rho(r) \propto r^{-2}$  over more than 0.1 pc in radius (e.g. Walker, Adams, & Lada 1990; Ladd et al. 1991; Motte et al. 1998). By contrast, the radial density profiles of isolated pre-collapse cores are found to flatten out near their centers, being much flatter than  $\rho(r) \propto r^{-2}$  at radii smaller than a few thousand AU (e.g. Ward-Thompson et al. 1994; AWM96). Such studies are of great interest to gain insight into the initial conditions of fast protostellar collapse (see Henriksen, André, & Bontemps 1997). So far, however, they have been essentially restricted to *isolated* protostars and dense cores. To some extent, our extensive 1.3 mm continuum mapping of the  $\rho$  Oph cloud allows us to tackle the same issues in a star-forming *cluster*. Because of complications arising from source multiplicity, we limit the present analysis to a selected sample of cores, clumps, and embedded protostars which have a relatively clean environment.

We follow a procedure similar to that described in AWM96 (see their Sects. 2.2 and 3.2.3). First, we average the emission of each source in circular annuli centered at the peak position. This yields a radial intensity profile  $I(\theta)$ , where  $\theta$  is the angular radius from source center. Owing to the small dust optical depth at 1.3 mm, the derived intensity profile is directly related to the column density profile and temperature gradient within the source. We assume that starless structures are roughly isothermal and that protostellar envelopes are centrally heated with temperature gradients approaching  $T(r) \propto r^{-0.4}$ . We then derive radial density profiles under the hypothesis of a spheroidal 3-D source geometry (see Sect. 3.2.3 of AWM96 for details). Since the dual-beam continuum mapping technique does affect the shape of the observed radial profiles, we use simulations to quantify the effect and make meaningful comparisons with simple input models such as power laws (see Motte et al. 1996).

The results obtained in this way on the mean radial structures of selected cores, clumps, and protostars are illustrated in Fig. 4 (see also Table 4).

Fig. 4a presents the circularly-averaged intensity profiles of the dense cores Oph-B2 and Oph-A. It can be seen that Oph-B2 contains a relatively large, flat inner region  $\sim 5000$  AU (i.e.,  $30''$ ) in radius, while its outer part is consistent with a  $\rho(r) \propto r^{-2}$  density law. By contrast, Oph-A is much more centrally condensed. Taken as a whole, its intensity profile is roughly consistent with an average radial density gradient  $\rho(r) \propto r^{-2}$  (see Fig. 4a). A similar overall  $r^{-2}$  density structure was reported earlier by Loren et al. (1983) on the basis of

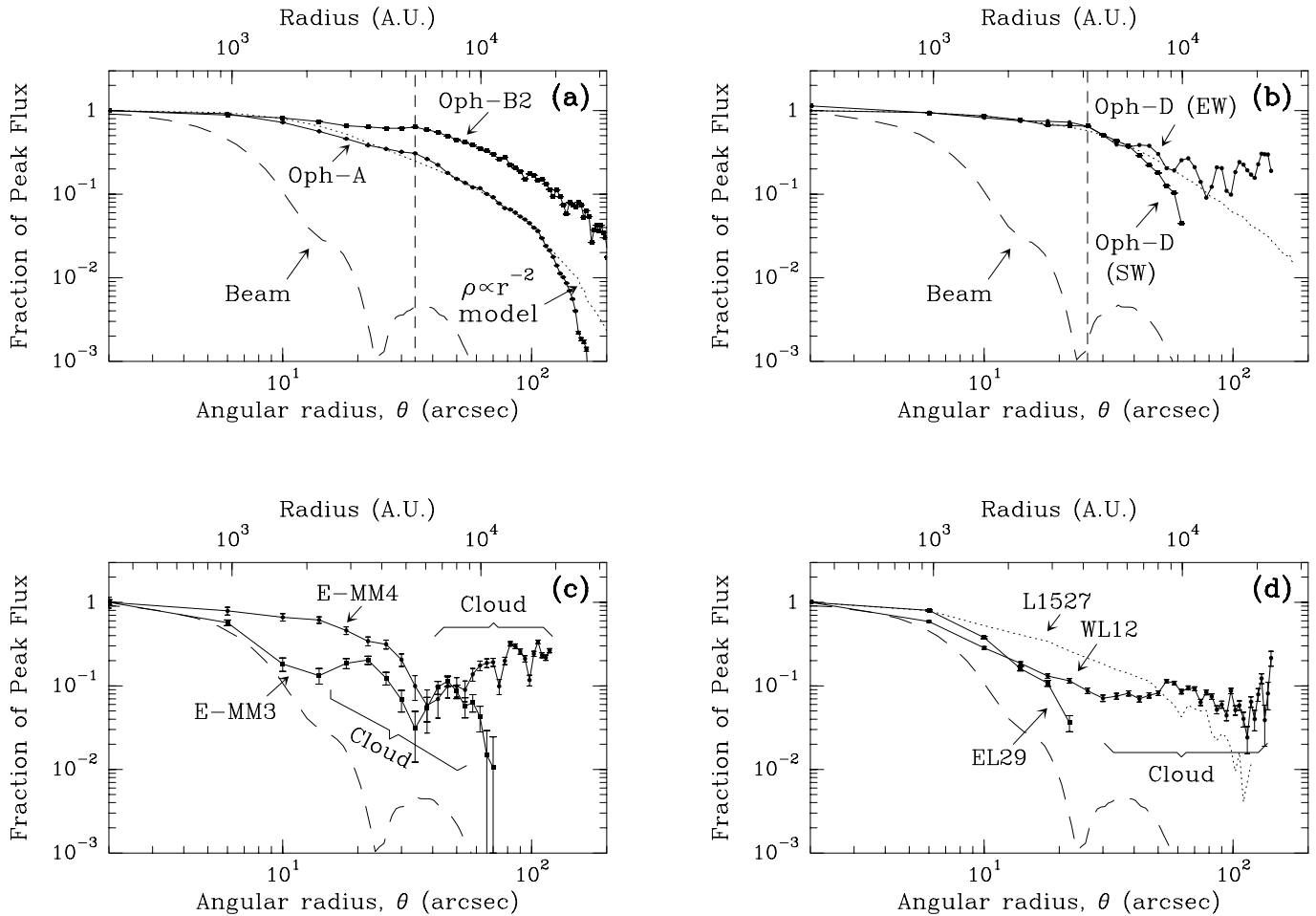


**Fig. 4a–d** Normalized radial intensity profiles of selected dense cores, starless clumps, and protostars. In all panels, the beam profile is shown as a long-dashed curve for comparison. In **a** and **b**, short-dashed vertical lines mark the radius inside which the inferred density gradients of Oph-B2 and Oph-D are flatter than  $\rho(r) \propto r^{-2}$ . **a** Azimuthally-averaged flux profiles of Oph-A and Oph-B2 (solid lines) compared with the simulated profile of a spherical isothermal model with  $\rho(r) \propto r^{-2}$  for  $r > 1000$  AU (dotted line). **b** East-west cut of the pre-stellar core  $\rho$  Oph-D, averaged along its major axis, compared with the intensity profile obtained by circularly averaging the south-west quadrant of the core. The dotted line shows a spherical, isothermal model with  $\rho(r) \propto r^{-2}$  for  $r > 4000$  AU (cf. L1689B in AWM96). **c** Azimuthally-averaged flux profiles of the starless clumps OphE-MM3 and OphE-MM4 (solid curves). **d** Azimuthally-averaged flux profiles of the two  $\rho$  Oph protostars WL 12 and EL 29 (solid lines), compared with the Taurus protostar L1527 (dotted line – see also map in Fig. 6b). (The 1.3 mm emission from EL 29 was averaged over the north-east side of the C<sup>18</sup>O ridge only, in order to avoid confusion from other sources.)

lower resolution molecular-line data. We point out, however, that the detailed density structure of Oph-A is clearly very far from a smooth power law since the core is fragmented in at least five strong protostellar clumps (see Fig. 2a).

To emphasize the fact that actual core shapes depart from simple spheres or ellipsoids in some cases, we show, in Fig. 4b, two distinct profiles for the Oph-D core. This starless core has a filamentary morphology and is clearly elongated in the south-west/north-east direction (P.A.  $\sim 30^\circ$  – see Fig. 2d). Fig. 4b displays a mean cut of the core through its minor axis, obtained by linear averaging along the major axis, as well a mean radial profile derived by circularly averaging the south-west quadrant of the source. Both profiles are relatively flat at small radii and are consistent with  $\rho(r) \propto r^{-2}$  only over a small radial extent beyond  $r \sim 4000$  AU (i.e.  $25''$ ). The minor-axis cut

merges with emission from the ambient cloud at a radius of  $\sim 13000$  AU (i.e.,  $80''$ ), but the south-west profile becomes significantly steeper than the  $\rho(r) \propto r^{-2}$  model (dotted line) at large radii. The latter feature, derived from 1.3 mm emission properties, is in qualitative agreement with the mid-IR absorption profiles of the core recently obtained with ISOCAM (Abergel et al. 1997). These results suggest that Oph-D possesses a sharp edge on its south-west side, possibly due to compression by an expanding shell from the Sco OB2 association (see also Sect. 6.3 below).

We have also derived azimuthally-averaged radial intensity profiles for the strongest and/or most isolated ‘starless’ clumps identified in Figs. 2a–2h (see Sect. 3.2.2 and Table 2). Several of these clumps, like OphE-MM4 shown in Fig. 4c, have a flat inner radial intensity profile reminiscent of starless cores (see, e.g., Oph-B2

**Table 4.** Density structure of DCO<sup>+</sup> cores and starless clumps

Clump name	$R_{flat}^{(1)}$ (AU)	$\langle n_{H_2} \rangle_{flat}^{(2)}$ (cm <sup>-3</sup> )	$M_{flat}^{(3)}$ ( $M_{\odot}$ )	Outer part <sup>(4)</sup>
Oph-B1	6 000	$1.2 \times 10^6$	0.9	$\rho(r) \propto r^{-2}$
Oph-B2	5 400	$3.2 \times 10^6$	4.8	$\rho(r) \propto r^{-2}$
OphC-S	3 400	$2.8 \times 10^6$	2.0	$\rho(r) \propto r^{-2}$
Oph-C	> 18 000	$1.5 \times 10^5$	7.4	edge ?
Oph-D	4 000	$9.0 \times 10^5$	0.9	EW: $\rho(r) \propto r^{-2}$ , then merging; SW: edge ?
Oph-A	$\sim 1\,000$	$3.0 \times 10^7$	0.6	$\rho(r) \propto r^{-2}$ up to 20 000 AU, then edge ?
Oph-E	> 16 000	$1.2 \times 10^5$	7.5	edge ?
Oph-F	$\sim 7\,000$	$5.5 \times 10^5$	1.9	Gaussian shape, edge ?
OphE-MM3	< 400	$2.0 \times 10^6$	0.08	unresolved $R_{flat}$ , merging at $\sim 2\,000$ AU
OphE-MM4	2 600	$5.5 \times 10^5$	0.4	edge, then merging at $\sim 6\,000$ AU ?

Notes:

- (1) Estimated radius of flat inner region.
- (2) Density averaged over flat inner region.
- (3) Mass of flat inner region as derived from 1.3 mm continuum data.
- (4) Inferred radial density profile for  $R > R_{flat}$ ; “edge ?” means profile must be significantly steeper than  $\rho(r) \propto r^{-2}$ .

in Fig. 4a), while others, such as OphE-MM3 (also shown in Fig. 4c), are more centrally peaked and do not exhibit any inner flattening. In all, we have identified 19 clumps of the former type and 10 clumps of the latter type, which are marked as ‘diffuse’ and ‘compact’ respectively in the last column of Table 2. The remaining 33 starless clumps of Table 2 cannot be classified as either ‘compact’ or ‘diffuse’ due to insufficient signal-to-noise and/or confusion with the surrounding environment. In Sect. 5.1 below, we suggest that the ‘diffuse’ clumps are pre-collapse in nature while the ‘compact’ clumps may be extremely young, collapsing protostars.

Finally, we stress that the protostellar envelopes detected in Fig. 1 around Class I and Class 0 YSOs appear to be very compact: they merge with dense cores, other envelopes, and/or the diffuse ambient cloud at a *finite* radius  $\lesssim 5\,000$  AU. This contrasts with the isolated protostellar envelopes observed in the Taurus cloud, which are virtually scale-free and often extended over more than  $\sim 30\,000$  AU in radius (e.g. Ladd et al. 1991, Motte et al. 1998). We illustrate this point in Fig. 4d which compares the radial profiles of the two  $\rho$  Oph Class I YSOs, WL 12 and EL 29, with that of the well-known Class 0 object L1527 in Taurus (see also Fig. 6b below).

Overall, our present results confirm the finding by Ward-Thompson et al. (1994) that pre-stellar density profiles differ markedly from protostellar profiles. This appears to be true both in isolated regions (e.g. Ward-Thompson et al. 1994) and in clusters (this paper).

The major difference between clusters like  $\rho$  Ophiuchi and isolated regions is that in clusters both protostellar envelopes and pre-collapse cloud fragments have compact, finite sizes of a few thousand AU.

## 5. Discussion: small-scale structures

### 5.1. Nature: circumstellar, protostellar, and pre-collapse clumps

Our 1.3 mm continuum mosaic (Fig. 1) provides a census of  $\sim 2\,000 - 4\,500$  AU (i.e.,  $\sim 15'' - 30''$ ) dust structures in the  $\rho$  Oph main cloud, which should be essentially complete down to a mass sensitivity limit of  $\sim 0.004 - 0.1 M_{\odot}$  (depending on the type of structure – see Sect. 3.1 above). In Sect. 3.2, we identified at least 100 fragments in the angular size-scale range of  $15'' - 30''$ . These small-scale dust structures include both circumstellar envelopes/disks around embedded YSOs and starless clumps, which we discuss in turn below.

We detect unresolved emission associated with the circumstellar disks of 14 Class II sources from the AM94 and Greene et al. 1994 (hereafter GWAYL) samples. We also detect compact circumstellar structures toward the 16 Class 0, Class I, and flat-spectrum YSOs listed by AM94 and GWAYL in the mosaiced region, except WL 6. These emission structures, which are generally spatially resolved (e.g. Fig. 4d), most likely correspond to spheroidal protostellar envelopes (see Terebey et al. 1993 and AM94). Besides VLA 1623 (AWB93), we identify only one other candidate Class 0 object more massive than  $0.1 M_{\odot}$  in the  $\rho$  Oph main region (LFAM 1, see Appendix A). In addition, based on their detections at 1.3 mm, we confirm the probable protostellar nature of two candidate Class I sources of CRBR and propose three more Class I candidates (see Table 3).

According to current interpretation, Class 0, Class I, and flat-spectrum sources represent various stages of accreting protostars for which  $L_{bol} \approx L_{acc} \approx G M_{*} \dot{M} / R_{*}$  (see AM94, Kenyon et al. 1993, Calvet et al. 1994, respectively). The to-

tal number of such accreting objects with  $M_{env} \gtrsim 0.03 M_{\odot}$  is thus  $\sim 21$  in the  $\sim 1 \text{ pc}^2$  surveyed area. Some of the Class I and flat-spectrum YSOs have surprisingly low bolometric luminosities ( $L_{bol} \lesssim 0.1 L_{\odot}$ , see GWAYL), however, suggesting they are slowly accreting (i.e.,  $\dot{M} \lesssim 10^{-7} M_{\odot} \text{ yr}^{-1}$ ), low-mass ( $M_{*} \lesssim 0.1 M_{\odot}$ ) objects (we assume  $R_{*} \approx 3 R_{\odot}$ ).

The 58 (non-composite) starless clumps of Table 2 range in total (gas + dust) mass from  $\sim 0.05 M_{\odot}$  to  $\sim 3 M_{\odot}$ , and in peak  $\text{H}_2$  density between  $\sim 4 \times 10^5 \text{ cm}^{-3}$  and  $2 \times 10^8 \text{ cm}^{-3}$ . We argue that these clumps are very likely gravitationally bound and either pre-stellar or protostellar in nature. First, the estimated clump masses are consistent to within a factor of 2 with the Jeans or Bonnor-Ebert critical mass (e.g. Bonnor 1956),  $M_{BE} = 2.4 R a_s^2 / G$  (where  $a_s$  is the isothermal sound speed), except for the clumps of Oph-B2 and the most massive clumps of Oph-A (see Table 2). In the latter cases, the 1.3 mm mass estimates are 2–10 times *larger* than the Jeans mass. Second, recent spectroscopic observations of the cloud with the IRAM 30-m telescope (Bacmann et al., in prep.) show that the clumps are characterized by very small levels of turbulence, except precisely those of Oph-B2 and Oph-A. In these observations, several clumps of Table 2 were detected in molecular lines such as  $\text{C}^{18}\text{O}(1-0)$  and  $\text{DCO}^+(3-2)$ . The observed line widths were typically  $\Delta V \lesssim 0.5 \text{ km s}^{-1}$  ( $\Delta V \lesssim 0.7 \text{ km s}^{-1}$  in Oph-A – see AWB93), indicative of one-dimensional velocity dispersions  $\sigma_{tot} \lesssim 0.3 \text{ km s}^{-1}$ , only slightly larger than the isothermal sound speed  $a_s \sim 0.2\text{--}0.3 \text{ km s}^{-1}$  of the cloud (for  $T \sim 10\text{--}20 \text{ K}$ ). These results suggest that most of the clumps are close to gravitational virial equilibrium with estimated  $M/M_{vir} \sim 0.3\text{--}0.5$  (see AWB93 for the Oph-A clumps). (Here,  $M_{vir}$  is the virial mass, equal to  $3 R \sigma_{tot}^2 / G$  and  $5 R \sigma_{tot}^2 / G$  for spherical clumps with  $\rho \propto r^{-2}$  and uniform density distributions, respectively.) This contrasts with the lower-mass ( $M < 0.1 M_{\odot}$ ), lower-density ( $n_{\text{H}_2} \sim 4 \times 10^5 \text{ cm}^{-3}$ ) clumps observed on similar size scales by Langer et al. (1995) in TMC1, which are gravitationally unbound by a large factor ( $M/M_{vir} < 0.1$ ). Recall that a clump remains gravitationally bound as long as  $M/M_{vir} > 0.5$  (e.g. Pound & Blitz 1993). Pending confirmation through more complete line observations, we conclude that the clumps we detect at 1.3 mm are generally bound and will probably form stars in the near future. We note, however, that most of the clumps of Table 2 are  $\lesssim 0.2 M_{\odot}$  features which can at best form very low-mass stars or brown dwarfs. Some of the least massive clumps may thus be proto-brown dwarfs (see Pound & Blitz 1993), but we cannot exclude that others are merely transient clumps.

We may go further and use the ‘compact’ or ‘diffuse’ 1.3 mm morphology of the starless clumps (see last column of Table 2 and Sect. 4) to divide them into two physically distinct groups. The ten clumps classified as ‘compact’ are well-defined, highly centrally condensed (see the example of OphE-MM3 in Sect. 4 and Fig. 4c), and have typical mean densities  $n_{\text{H}_2} \sim 10^7\text{--}10^8 \text{ cm}^{-3}$ . They may be considered as candidate ‘isothermal protostars’, i.e., collapsing cloud fragments with no central hydrostatic stellar core (see, e.g., Mezger et al. 1992a). Recall that collapse models which start from non-singular initial conditions predict the existence of an isothermal phase of dynamical col-

lapse building up a strong central concentration of matter *before* the beginning of the YSO accretion phase (e.g. Larson 1969; Tomisaka 1996; Henriksen, André, & Bontemps 1997; Basu 1997). Some of the ‘compact’ clumps may be in this ‘runaway’ collapse phase although this remains to be confirmed by observations of appropriate spectral line signatures. (Despite their centrally peaked 1.3 mm morphology resembling that of Class 0 protostars, the compact clumps are unlikely to be new Class 0 sources since, contrary to most known Class 0 protostars, they are *not* associated with VLA radio continuum emission – see LFAM.)

By contrast, the 19 clumps classified as ‘diffuse’ in Table 2 are less centrally concentrated and less dense (with mean densities  $n_{\text{H}_2} \sim 8 \times 10^4\text{--}8 \times 10^6 \text{ cm}^{-3}$ ) than the ‘compact’ clumps. When the signal-to-noise is high enough for a detailed radial structure study, the averaged intensity profiles of these clumps appear to flatten out near the centers (see the example of OphE-MM4 in Fig. 4c and Sect. 4), a property reminiscent of isolated pre-stellar cores (Ward-Thompson et al. 1994, AWM96). We thus suggest that the ‘diffuse’ clumps are pre-collapse structures in rough hydrostatic equilibrium.

Although it is clearly premature to infer absolute timescales at this point, the relative numbers of sources present in the various groups of small-scale 1.3 mm structures suggest that, in the  $\rho$  Oph main cloud, the starless clump phase may be  $\sim 3$  times as long as the Class I phase, and the isothermal collapse phase somewhat longer than the Class 0 phase. The latter would be in qualitative agreement with the scenario of induced collapse proposed by Henriksen et al. (1997) which predicts that the isothermal phase should last for a significant fraction of the total collapse/accretion time.

## 5.2. Mass distribution of the pre-stellar clumps

The mosaic of Fig. 1 is remarkable in that it probes pre-collapse clumps, collapsing/accreting protostars, and post-collapse circumstellar structures *simultaneously*. Therefore, it allows us to establish a *continuity between pre-stellar dense clumps and young stars*.

With this in mind, we plot, in Fig. 5, the mass distribution of 58 starless clumps listed in Table 2. We here exclude the four composite clumps of Table 2, but include the two candidate Class 0 protostars VLA 1623 and LFAM1 (since most of the mass is still in the protostellar envelope rather than in the central star at the Class 0 stage, these objects effectively resemble compact clumps). The plotted quantity,  $\Delta N / \Delta m$ , is the number of clumps per unit mass counted in each mass bin, which we compare with power laws of the type  $\Delta N / \Delta m \propto m^{-\alpha}$ . It can be seen that the observed clump mass spectrum is relatively shallow, with a slope  $\alpha \sim 1.5$ , in the  $0.1\text{--}0.5 M_{\odot}$  mass range, but that it steepens to  $\alpha \sim 2.5$  in the higher ( $0.5\text{--}3 M_{\odot}$ ) mass range. Note that the shape of this mass spectrum is not affected by the factor of  $\sim 2$  uncertainty on the absolute value of the dust mass opacity (Sect. 3.1), providing  $\kappa_{\nu, 1.3\text{mm}}$  does not vary from clump to clump. Furthermore, the mass spectrum remains qualitatively unchanged if a ‘pre-stellar’ opacity is used for the two Class 0

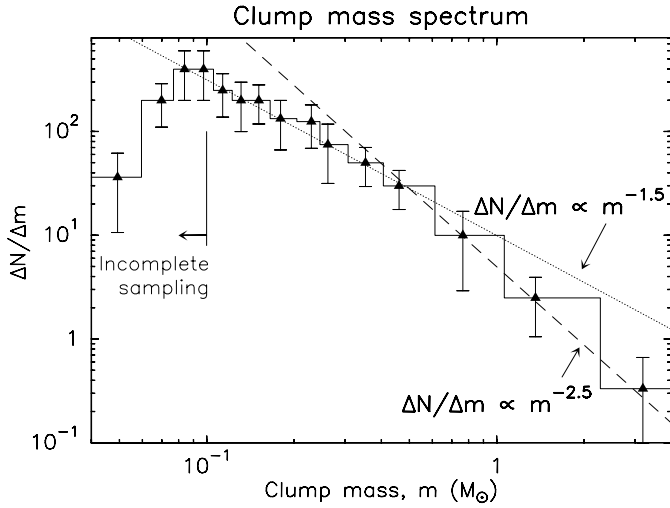


**Fig. 5.** Frequency distribution of masses for 60 small-scale clumps extracted from the mosaic of Fig. 1 (solid line). The dotted and long-dashed lines show power laws of the form  $\Delta N/\Delta m \propto m^{-1.5}$  and  $\Delta N/\Delta m \propto m^{-2.5}$ , respectively. The error bars correspond to  $\sqrt{N}$  counting statistics.

objects or if a “protostellar” opacity is used for the ten centrally condensed clumps.

The mass distribution seen in Fig. 5 for *clumps* mimics the behavior of the *stellar* initial mass function (IMF), which is known to have  $\alpha \sim 2.5$  for  $1 M_{\odot} \lesssim M_{\star} \lesssim 10 M_{\odot}$  (e.g. Salpeter 1955) and  $\alpha \sim 1.5$  for  $M_{\star} \lesssim 1 M_{\odot}$  (e.g. Miller & Scalo 1979, Güsten & Mezger 1983), with a possible maximum at  $\sim 0.3 M_{\odot}$  (Scalo 1986, Strom et al. 1993).

Recall that, by contrast, all molecular-line studies conducted up to now have found a shallow clump mass spectrum with a single slope  $\alpha \sim 1.5$  at all masses (e.g. Blitz 1993, Loren 1989), which differs qualitatively from the stellar IMF. Interestingly enough, the mass spectrum we derive when we consider small-scale clumps *and* larger-scale cores together is also consistent with  $\alpha \sim 1.5$ .

The above results suggest that there may be a direct relation between clump mass and stellar mass at the length scale of  $\sim 2000 - 4500 \text{ AU} \sim 0.01 - 0.02 \text{ pc}$  (i.e.,  $\sim 15'' - 30''$  in  $\rho$  Oph). While existing line studies may not have the resolution and/or sensitivity to resolve dense cores into small-scale clumps, our 1.3 mm continuum mosaic may be resolving structures corresponding to the *direct progenitors of individual stars or systems*. In this view, stars would form from bounded clumps of finite masses (as indeed suggested by the radial profiles shown in Fig. 4c), and most of the ‘initial’ clump masses (i.e., masses at the onset of collapse) would end up in stars, resulting in a high star formation efficiency. If the above is true, it would imply that the physics of fragmentation is essential in determining the final masses of forming stars (i.e., the IMF) in clustered regions like the  $\rho$  Oph main cloud. This would be in agreement with some theoretical scenarios of protocluster formation (e.g. Larson 1985, Zinnecker 1989). Such a picture need not be universal, however, and is in fact unlikely to apply to regions of

more isolated star formation like the Taurus cloud. In these regions, protostars may accrete from larger (effectively infinite) reservoirs of mass, and other processes such as stellar winds may be more important in limiting accretion and defining stellar masses (e.g. Shu et al. 1987). It would thus be very instructive to derive the clump mass spectrum in other star-forming regions using the same technique as the one employed here, in order to assess the importance of cloud-to-cloud variations.

## 6. Discussion: relation to large-scale cloud properties

### 6.1. Cloud fragmentation

We have used our dust continuum data to estimate the fragmentation lengthscale characterizing the  $\rho$  Oph cores in two ways. First, we have estimated the mean separation between the clumps/YSOs present in each core by dividing the total surface area of the core by the number of clumps/YSOs. This yields a diameter ranging from  $\sim 6000 \text{ AU}$  to  $\sim 10000 \text{ AU}$ , the shortest value being measured in the densest cores, i.e., Oph-A, Oph-B2, OphC-S.

Second, we have considered several filamentary-like structures seen in our maps (see white lines and curves in Fig. 1 and Figs. 2a-2f). In particular, one may notice the linear string of 11 clumps/YSOs detected in the southern part of the  $\text{C}^{18}\text{O}$  ridge of WL83 and the cloud fragments aligned along the major axes of Oph-B1, OphC-S, and Oph-D. Along these filaments, the average projected distance between objects is shorter than above and ranges from  $\sim 4000 \text{ AU}$  (i.e.,  $\sim 25''$  at 160 pc) to  $\sim 8000 \text{ AU}$  (i.e.,  $\sim 50''$ ).

Cloud fragmentation lengthscales of this order are consistent with the finite  $\lesssim 5000 \text{ AU}$  outer radius estimated for several clumps and protostellar envelopes in Sect. 4 (see Fig. 4). We also note that the FWHM short sizes of the various filaments is of the same order. In the following, we will thus adopt a representative value  $L = 6000 \text{ AU}$  for the fragmentation lengthscale in the  $\rho$  Oph main cloud.

Such a lengthscale is clearly shorter than the fragmentation lengthscale observed in the Taurus cloud. In Taurus, protostars generally form in isolation and the median nearest-neighbor distance between T Tauri stars is estimated to be  $\sim 50000 \text{ AU}$  (Gomez et al. 1993). This difference is illustrated in Fig. 6 which compares the region surrounding EL 29 in Oph-E with the well-known L1527 protostar in Taurus (e.g. Ladd et al. 1991, Motte et al. 1998). A similar trend can be seen on the radial intensity profiles shown in Fig. 4d (see Sect. 4 above).

A short pre-collapse fragmentation lengthscale in the parent cloud can strongly influence the evolution of any protostar forming in that cloud by limiting the radius of its ‘sphere of influence’. For instance, in the context of the inside-out collapse theory of Shu et al. (1987), the collapse expansion wave would reach the outer boundary of a typical  $\rho$  Oph pre-stellar clump in a time  $t = L/2a_s \sim 1 \times 10^5 \text{ yr}$ , which is shorter than the typical Class I lifetime (i.e.,  $\sim 2 \times 10^5 \text{ yr}$  according to WLY and GWAYL). This may explain why, in  $\rho$  Oph, Class I sources generally seem to have passed the main accretion phase and to be in a phase of residual accretion/ejection (see Henriksen et al.

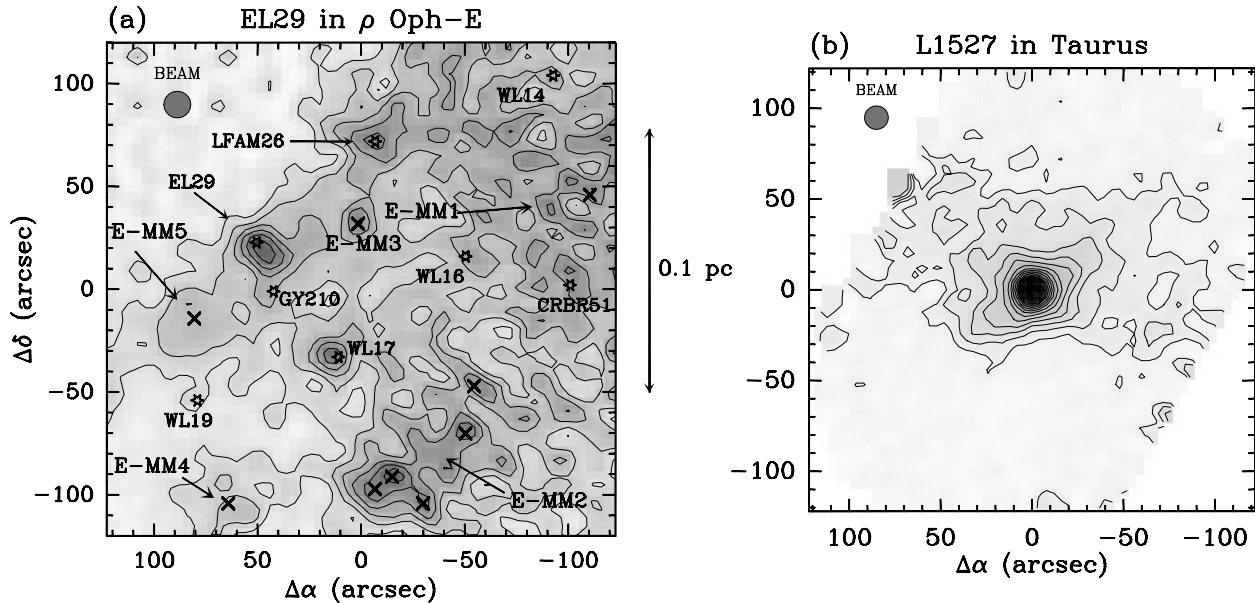


**Fig. 6a and b** Comparison of the immediate 1.3 mm continuum environment of the Class I source EL 29 in  $\rho$  Oph-E (a) with that of the Class 0 source L1527 in Taurus (b). Contour levels go from 20 to 420 mJy/13''-beam by 20 mJy/13''-beam. A *common* 0.1 pc scale is displayed. YSOs and clumps are denoted by star markers and crosses, respectively. Mean rms noise level is  $\sim 6$  mJy/13''-beam in **a** and  $\sim 5$  mJy/13''-beam at map center in **b**. While the environment of EL 29 is complex and highly structured, that of L1527 is dominated by a *single* circumstellar envelope perturbed by an outflow oriented east-west.

1997). In agreement with this view, the present mapping study confirms the claim made by AM94 that  $\rho$  Oph Class I sources have small circumstellar masses ( $\lesssim 0.1\text{--}0.3 M_{\odot}$  at most) and have thus already accreted the bulk of their final stellar mass in contrast to Class 0 objects.

It is noteworthy that the filamentary structures detected in our maps (see Fig. 1 and Figs. 2a-2f) are quasi-periodic. Similar features have also been reported in other regions (e.g. Schneider & Elmegreen 1979, Mezger et al. 1992a, Langer et al. 1995, Chini et al. 1997). Several theoretical explanations exist in the literature that could potentially account for such filamentary-like, periodic structures.

In primarily magnetically supported molecular clouds, the decay of short hydromagnetic waves due to ambipolar diffusion can initiate fragmentation and the formation of clumps along static magnetic flux tubes (e.g. Mouschovias 1991). This mechanism predicts a typical number of 3–5 fragments aligned along critical flux tubes. In the  $\rho$  Oph case, however, recent Zeeman and polarimetric observations suggest that the static magnetic field is too weak ( $< 10\text{--}20 \mu\text{G}$ , Troland et al. 1996) and its geometry too complex (Sato et al. 1988, Goodman & Heiles 1994) for (static) magnetic forces to be dynamically important. Carlberg & Pudritz (1990) have investigated a variant of the above MHD process when the fluctuating (wave) component of the magnetic field dominates the static component, a situation probably appropriate to the  $\rho$  Oph main cloud. Their simulations show that filamentary structures do develop in this case too, but that they are randomly oriented in contrast to the linear structures seen in Fig. 1 and Figs. 2a-2f (except in Oph-B2). Furthermore, the characteristic fragmentation length-

scale predicted by these MHD processes is the Alfvén length,  $\lambda_A \simeq 400 \text{ AU} \times \left(\frac{B}{20 \mu\text{G}}\right) \times \left(\frac{n_{\text{neutral}}}{10^5 \text{ cm}^{-3}}\right)^{-1}$  (see Mouschovias 1991), which is typically  $\sim 15$  times smaller than the observed 6 000 AU lengthscale.

Alternatively, even in the absence of strong magnetic fields, flattened or filamentary configurations can form as a result of cloud compression by external agents such as expanding HII regions or stellar wind shells. The collapse of such compressed layers/filaments is known to be highly unstable to fragmentation (e.g. Bastien et al. 1991). In these non-magnetic scenarios (e.g. Larson 1985, Whitworth et al. 1994, Bonnell et al. 1996), the typical fragmentation lengthscale and typical separation between fragments are both of order the Jeans length  $\lambda_J \simeq 7300 \text{ AU} \times \left(\frac{T}{15 \text{ K}}\right)^{1/2} \times \left(\frac{n}{10^5 \text{ cm}^{-3}}\right)^{-1/2}$ . In this view, the density enhancement necessary to reproduce the observed fragmentation lengthscale is  $n_{\text{H}_2} \sim 1.5 \times 10^5 \text{ cm}^{-3}$ , which corresponds to the lowest core density in Table 1 and is thus plausible.

We therefore conclude that the fragmentation observed in the  $\rho$  Oph main cloud most likely results from processes linked to the Jeans gravitational instability, with little influence of the magnetic field.

## 6.2. Comparison of the cloud cores

Clear differences can be seen among the  $1\text{--}6 \times 10^4$  AU cores of Sect. 3.2.1 and Figs. 2a–h. First, we distinguish between ‘passive’ and ‘active’ cores based on the YSO surface densities listed in Table 1. We define as ‘passive’ the cores for which the estimated YSO surface density is less than 1 star/(0.1 pc) $^2$ , i.e., less than the average surface density of mid-IR sources in the entire

$\rho$  Oph ISOCAM image (Abergel et al. 1996, Bontemps, Nordh, Olofsson et al. 1998). Such a low surface density suggests that no or little star formation has occurred in the core, if we account for the number of YSOs that may be either background or foreground to it.

By contrast, we call ‘active’ those cores whose YSO surface density is larger than  $2 \text{ stars}/(0.1 \text{ pc})^2$ . These cores have a significant excess of mid-IR sources with respect to the background  $\rho$  Oph field, indicating that several Class I and/or Class II objects must have formed in their interiors (Oph-A, Oph-E, and Oph-F).

Next, we compare the structures of passive and active cores. The densest passive cores (i.e. Oph-B1, Oph-B2, OphC-S, and Oph-D) have averaged radial intensity profiles which are flat in their inner parts (see Sect. 4 and Figs. 4a–b), a feature also observed in isolated pre-stellar cores (Ward-Thompson et al. 1994). As we expect pre-stellar cores to approach higher degrees of central concentration before forming stars (e.g. Larson 1969, Ciolek & Mouschovias 1994), we suggest that the radius  $R_{flat}$  of the flat inner region may be used as a rough indicator of core evolution (prior to dynamical collapse). According to this criterion, OphC-S and Oph-D, which have smaller values of  $R_{flat}$  (see Table 4), would be more evolved and closer to forming stars than Oph-B1 and Oph-B2.

In contrast, the active cores display a wide variety of mean radial density structures, including a  $\rho \propto r^{-2}$  power law gradient (Oph-A), a broad clumpy plateau (Oph-E), and a Gaussian-shaped profile (Oph-F). None of them shows the typical structure of pre-stellar cores, i.e., a large central region with a flat density gradient surrounded by a  $\rho \propto r^{-2}$  envelope (see Table 4).

The fraction of core mass within small-scale clumps does not seem to correlate with the passive or active state of the cores (see Fig. 7). In fact, Fig. 7 shows that the denser a core is, the more of its mass is distributed in clumps, independently of whether the core is forming stars or not. This suggests that the efficiency of the fragmentation process increases with core density. It is apparently not the number of starless clumps within the core FWHM area which increases with core density, but rather the average mass per clump. In particular, the typical clump mass is significantly larger in the denser cores Oph-A ( $1 M_{\odot}$ ) and Oph-B2 ( $0.4 M_{\odot}$ ) than in the other cores ( $\sim 0.2 M_{\odot}$ ). Furthermore, the lowest mass clumps of Oph-A are found near the edge of the core, where the density is one or two orders of magnitudes lower than in the center.

Finally, we comment on the relative evolutionary states of the active cores Oph-A and Oph-F by comparing, in both cases, the fraction of core mass within starless clumps and YSOs to the fraction of mass within starless clumps alone. To estimate the total mass contained in YSOs for each core, we assume that the median stellar mass of objects formed in  $\rho$  Oph is  $\sim 0.5 M_{\odot}$  (see Greene & Meyer 1995). In both cases about 40% of the total core mass is comprised in small-scale ( $15'' - 30''$ ) structures, but most of these structures are circumstellar in Oph-F (accounting for 30% of the core mass), and starless in Oph-A (see Fig. 7). Moreover, the fact that the surface density of near-/mid-IR YSOs

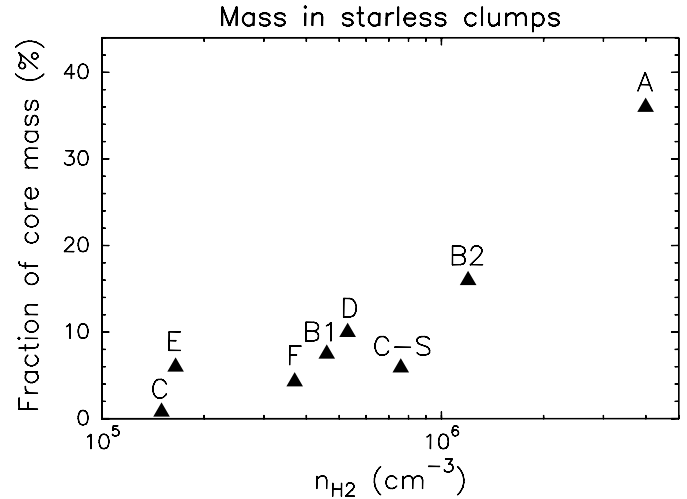


**Fig. 7.** Percentage of core mass in starless clumps as a function of peak core density.

in Oph-A increases when a larger core area is considered (see Table 1) suggests that star formation started in its outer part first and is progressing inward. This is consistent with a scenario in which fragmentation and collapse in Oph-A have only recently been induced by external factors (see Sect. 6.3). By comparison, Oph-F has a larger surface density of infrared YSOs which peaks near its center, suggesting it has been forming stars for a longer time than Oph-A.

### 6.3. Evidence for cloud compression and induced star formation

There is good evidence that several parts of the  $\rho$  Oph cloud have been compressed, resulting in induced star formation. Cloud collapse can be triggered by an increase in external pressure due to shocks associated with stellar wind shells, supernova remnants, or expanding HII regions (e.g. Woodward 1978, Elmegreen & Elmegreen 1978, Boss 1995). All three types of triggers appear to be present in  $\rho$  oph or its vicinity.

On large scales, the morphology, kinematics, and magnetic field configuration of the  $\rho$  Oph complex suggest a scenario in which an expanding shell of HI gas created by stellar winds and supernova explosions in the Sco OB2 association propagates from the rear, south-west to the front, north-east of the cloud (e.g. Vrba 1977, de Geus 1992). The shell would be powered by the most massive ( $\sim O7$ ) star(s) of the Sco OB2 association, which is located  $\sim 40$  pc behind, and to the south-west of, the  $\rho$  Oph star-forming region (de Geus 1992). The shell expansion would thus compress the (rear) south-western side of the molecular cloud, which is consistent with the low-resolution  $^{13}\text{CO}$  map of Loren (1989). The  $\rho$  Oph streamers may represent pre-existing cloud filaments ahead of the compression front, and the two cores, L1688 and L1689, massive accumulations of material swept up by the shock (Loren & Wootten 1986). Direct evidence for the presence of a slow shock in the interstellar medium surrounding the  $\rho$  Oph cloud has been found in the

form of a  $\lesssim 10 \text{ km s}^{-1}$  velocity difference between optical absorption lines of CH and CH<sup>+</sup> (Meyers et al. 1985, de Geus 1992). The velocity of the ‘transmitted’ shock inside the dense ( $n_{\text{H}_2} \gtrsim 10^5 \text{ cm}^{-3}$ ) main molecular cloud is probably in the range  $\sim 1\text{--}10 \text{ km.s}^{-1}$ . Interestingly, a slow ( $\lesssim 25 \text{ km s}^{-1}$ ), isothermal shock is precisely required to induce low-mass star formation, while stronger adiabatic shocks tend to disrupt molecular clouds before any star formation (e.g. Boss 1995, Foster & Boss 1996). Finally, we note that the small age dispersion ( $\lesssim 2 \times 10^6 \text{ yr}$ ) of both B stars and low-mass stars in the Sco OB2 association has been interpreted in the context of star formation triggered by the above-mentioned expanding shell (Walter et al. 1994).

On smaller scales, several features seen in our 1.3 mm continuum mosaic are also suggestive of induced star formation. Most of the linear structures shown in Figs. 2a-2f, especially the linear chain of embedded YSOs marked in Fig. 1, are roughly perpendicular to the direction of shock propagation proposed by Vrba (1977) and de Geus (1992). Remarkably, all the YSOs lying along the string of Fig. 1 have relatively strong 1.3 mm continuum emission and are also detected by the VLA in free-free radio continuum (LFAM), suggesting they are relatively young Class I protostars, i.e.,  $\sim 10^5$  years old. Dividing the chain length,  $\sim 0.5 \text{ pc}$ , by the sound speed,  $\lesssim 0.3 \text{ km s}^{-1}$  (for  $T \lesssim 25 \text{ K}$ ), yields a sound crossing time  $\gtrsim 1.5 \times 10^6 \text{ yr}$ , which is an order of magnitude longer than the estimated age of the sources. It is thus tempting to speculate that a supersonic trigger has synchronized the formation of this young alignment of protostars. The transmitted shock associated with the Sco OB2 expanding shell could do the job if its velocity is  $\gtrsim 3 \text{ km s}^{-1}$ . In this view, the shock front would now be somewhere to the north-east of the line of YSOs drawn in Fig. 1, perhaps between Oph-B1 and Oph-B2 as suggested by Loren & Wootten (1986). This would be consistent with the fact that Oph-B1, Oph-B2, OphC-S, and Oph-D have not yet started to form stars in contrast to the active cores Oph-E, Oph-F, and Oph-A. It would also agree with the suggestion made in Sect. 6.2 that OphC-S is more evolved than Oph-B1 and Oph-B2.

A difficulty, however, with this scenario, is that the south-eastern side of the 1.3 mm continuum ridge is much steeper than the south-western side (see Fig. 1). Such an asymmetry is *not* consistent with a shock propagating from the south-west to the north-east, even in the case of a magnetized C shock (Chièze, private communication). Projection effects could perhaps account for this asymmetry. One may notice that the broad Oph-E plateau includes two linear clumpy features marked as white lines in Fig. 2e (also visible in C<sup>18</sup>O – see Fig. 3a) which are roughly perpendicular to the alleged direction of the shock. Although these two elongated structures lie next to each other in projection onto the sky, the westernmost filament (along OphE-MM1 and MM2) could be closer to the front side of the cloud, which would explain that it is mostly pre-stellar and probably less evolved than the easternmost filament including the Class I YSOs EL 29 and LFAM 26. In this view, the Sco OB2 shell arriving from behind would have hit the easternmost filament before the westernmost filament. With similar projection ef-

fects, compression due to the expanding Sco OB2 shell could also account for the sharp south-western edge of Oph-D (see Fig. 4b and Sect. 4), assuming this core is located near the rear side of the cloud.

Further evidence for induced fragmentation and collapse is provided by comparison of our 1.3 mm continuum mosaic with the recent ISOCAM images of the cloud (e.g. Abergel et al. 1996). In particular, we note that, in projection, the six protostellar clumps OphA-MM7, OphA-MM6, SM1N, SM1, SM2, and OphA-MM8 lie almost exactly along the photodissociation front of the PDR region illuminated by the young B3 star S1 (see Figs. 2a and, e.g., André et al. 1988). The position of this PDR front is nicely delineated by the edge of the  $6.75 \mu\text{m}$  ISOCAM emission arising from the S1 compact HII region (emission probably dominated by PAH-like features – see Cesarsky et al. 1996). This remarkable spatial coincidence suggests that the six protostellar clumps seen at 1.3 mm formed by fragmentation in the compressed gas layer at the interface between the PDR and the Oph-A cloud core. Likewise, the group of embedded YSOs around GSS30-IRS1 may have formed as a result of interaction between the more evolved HII region associated with the B2V star HD 147889 (Schlickeiser et al. 1989 and references therein) and the  $\rho$  Oph cloud. (The photodissociation front corresponding to the HD 147889 PDR is seen as a prominent, curved  $6.75 \mu\text{m}$  emission feature by ISOCAM – see Fig. 1 of Abergel et al. 1996.)

## 7. Summary and conclusions

We have mosaiced the 1.3 mm dust continuum emission from a large ( $\sim 1 \text{ pc}^2$ ) portion of the  $\rho$  Ophiuchi central cloud using the IRAM 30-m telescope and the MPIfR bolometer array. Our main results and conclusions may be summarized as follows:

1. Our 1.3 mm continuum mosaic (Fig. 1) is simultaneously sensitive to small-scale ( $\sim 15''\text{--}30''$ ) and large-scale ( $1'\text{--}6'$ ) dust structures. The large-scale structures correspond to the 7 DCO<sup>+</sup> cores studied by Loren et al. (1990) and to 6 new, more diffuse cores (see Table 1). The 100 structures detected on small scales have deconvolved diameters  $\sim 1000\text{--}4000 \text{ AU}$  and are associated with 59 starless clumps (Table 2) and 41 circumstellar envelopes/disks around embedded YSOs (Tables 3 and 5).
2. Comparison of the masses derived from the 1.3 mm continuum with Jeans and virial masses suggests that most of the 59 starless clumps are gravitationally bound and may form stars or brown dwarfs in the near future. These clumps range in mass between  $M \sim 0.05 M_{\odot}$  and  $\sim 3 M_{\odot}$ , and in mean density between  $n_{\text{H}_2} \sim 4 \times 10^5 \text{ cm}^{-3}$  and  $\sim 2 \times 10^8 \text{ cm}^{-3}$ .
3. We identify only one new candidate Class 0 protostar with  $M_{\text{env}} > 0.1 M_{\odot}$  besides VLA 1623. Ten starless clumps display a centrally condensed morphology and may be considered candidate isothermal protostars, i.e., collapsing cloud fragments with no central hydrostatic core. Nineteen other clumps have relatively flat inner intensity profiles, suggesting they are pre-collapse structures similar to, but more

compact than, the isolated pre-stellar cores studied by Ward-Thompson et al. (1994).

4. The mass distribution of the pre-stellar clumps follows approximately  $\Delta N/\Delta m \propto m^{-1.5}$  below  $\sim 0.5 M_{\odot}$ , which is similar to the clump mass spectrum found by large-scale molecular line studies (e.g. Blitz 1993). However, the observed clump mass spectrum appears to steepen to  $\Delta N/\Delta m \propto m^{-2.5}$  above  $\sim 0.5 M_{\odot}$ . This approaches the slope of the *stellar* initial mass function, suggesting the clumps we detect may be the direct precursors of individual stars or systems.
5. The typical fragmentation lengthscale derived from the average separation between clumps or embedded YSOs in our  $\rho$  Oph 1.3 mm mosaic is  $\sim 6\,000$  AU. This contrasts with the Taurus cloud where dense cores and young stars are generally isolated over much larger distances  $\gtrsim 30\,000$  AU. The short lengthscale observed in  $\rho$  Oph is consistent with various scenarios for fragmentation in compressed layers/filaments based on the Jeans gravitational instability (e.g. Larson 1985, Whitworth et al. 1994).
6. In agreement with (5), the circumstellar envelopes surrounding  $\rho$  Oph Class I and Class 0 YSOs are found to be compact, merging with other envelopes/cores and the ambient cloud at a finite radius  $\lesssim 5\,000$  AU (i.e.,  $30''$ ). This is  $\gtrsim 3$  times smaller than both typical protostellar envelopes in Taurus and the collapse expansion wavefront at a ‘Class I age’ of  $\sim 2 \times 10^5$  yr in the standard theory of isolated protostars (Shu et al. 1987).
7. There is ample, albeit mostly circumstantial, evidence that cloud fragmentation and low-mass star formation have been induced in the  $\rho$  Oph central cloud by various agents such as a supernova/wind shell arriving from the Sco OB2 association and two expanding HII regions from the B2–B3 stars HD 147889 and S1.
8. Points 4, 5, 6, and 7 emphasize the fact that the self-similar theory of quiescent, low-mass star formation developed by Shu and co-workers for clouds like Taurus is not appropriate to describe protostellar collapse in the  $\rho$  Oph cluster. Instead, our  $\rho$  Oph observations favor a picture in which collapse is initiated in bounded dense clumps resulting from fragmentation, and individual stars are built from finite reservoirs of mass. In this case, the scenario advocated by Foster & Chevalier (1993) and Henriksen et al. (1997), which predicts a strong decline of accretion/ejection at the beginning and end of the main accretion phase, is likely to provide a better description of individual protostellar collapse.

*Acknowledgements.* We would like to thank Isabelle Ristorcelli and Sylvain Bontemps for kindly communicating their PRONAOS and ISOCAM results prior to publication. We are grateful to Bruce Wilking for making his  $C^{18}O$  map available to us. We acknowledge enlightening discussions with Jean-Pierre Chièze on the structure of shocked clouds. We also thank Sylvain Bontemps, Thierry Montmerle, and Sue Terebey for useful comments.

## Appendix A: comparison with circumstellar fluxes of AM94

To make meaningful comparisons with the YSO flux densities estimated by AM94 on the basis of ON-OFF measurements, we have extracted the circumstellar emission associated with each YSO from the surrounding background emission detected in the 1.3 mm continuum mosaic (see description of subtraction procedure in Sect. 3.2). This yields fluxes which are generally in good agreement with those published by AM94 (see Table 5).

A few objects deserve individual comments. The sources WL 19, IRS 46, and IRS 51 have somewhat stronger continuum fluxes here than in AM94. This is probably due to the fact that the WLY positions used by AM94 in their ON-OFF observations of these objects are apparently off by  $\simeq 5''$ . The region around the star SR 21 was mapped here under relatively bad weather conditions implying an uncertain calibration which could account for the disagreement observed in Table 5.

The measurements of AM94 for YSOs lying close to VLA 1623 and LFAM 1 were confused by the strong emission associated with these two sources. The present mosaic allows us to clarify the situation in several cases: we now have a positive detection for LFAM 3, we confirm the detection of GSS30-IRS1, and we can assign significantly lower 1.3 mm upper limits to the fluxes of GSS 32, GY 10, and GY 11 (see Table 5).

The multiple system (IRS 37, WL 3, WL 4, WL 5) lying between Oph-B1 and Oph-B2 appears to consist of four extinguished pre-main sequence (Class II/III) stars with no significant intrinsic 1.3 mm emission.

Last but not least, we identify the VLA object LFAM 1 as a possible new, low-mass Class 0 protostar. First, the 1.3 mm emission of LFAM 1 is compact but spatially resolved, suggesting the presence of a circumstellar envelope (as opposed to just a disk). Second, the integrated 1.3 mm flux we measure for this object is  $S_{1.3}^{int} \approx 400$  mJy, while its bolometric luminosity is estimated to be  $L_{bol} \lesssim 0.2 L_{\odot}$  by GWAYL. This results in a ratio  $S_{1.3}^{int}(160pc)/L_{bol} \gtrsim 2$  Jy/ $L_{\odot}$ , which is well above the limiting value of  $\sim 0.2$  Jy/ $L_{\odot}$  for Class I objects (e.g. André 1996). Thus, LFAM 1 is an excellent candidate for being a YSO in which the circumstellar envelope mass exceeds the central stellar mass (see AWB93).

## Appendix B: dual-beam continuum filtering and comparison with line observations

Since our 1.3 mm continuum mosaic (Fig. 1) was obtained by combining a large number of small maps taken in the dual-beam mapping mode, it is intrinsically insensitive to structures more extended than the typical size of an individual bolometer map in azimuth, i.e.,  $\sim 4.5'$  (see Emerson et al. 1979). Based on simulations of the bolometer-array observations (see Motte et al. 1996) which use the  $C^{18}O$  map of WL83 as an input model, we estimate that this effect is not large for the compact cores Oph-A, Oph-B1, Oph-B2, OphC-S, Oph-D, and Oph-F, but quite significant for the broad cores Oph-C and Oph-E. Quantitatively, Oph-A, Oph-B1, Oph-B2, OphC-S, and Oph-F lie over a wide ( $> 5'$ )  $C^{18}O$  emission plateau (see Fig. 3a) with  $\langle N_{H_2} \rangle \sim 2-3 \times 10^{22}$  cm $^{-2}$  which corresponds to  $\sim 1/4$  of the peak  $C^{18}O$

**Table 5.** Point-source extraction and comparison with YSO fluxes of AM94

Source Name	$S_{1.3mm}^{peak}$ (mJy/beam) AM94	$S_{1.3mm}^{los}$ (mJy/beam) (1)	Background (mJy/beam) (2)	$S_{1.3mm}^{peak}$ (mJy/beam) (3)	Class, comments and references (4)
DoAr21	<5	<30	none	<30	IIID
GSS26	120	140	~15	125±20	II
GSS29	<15	<10	none	<10	II
DoAr24	<25	<30	none	<30	II
GSS30-IRS1	100	130	40±20	90±30	I
LFAM1/GSS30-IRS3	260	265	<20	250±20	0?
GSS30-IRS2	<90	70	~70	<20	III
GY10	75	75	~75	<10	?, 13'' NW of OphA-MM2
GY11	<50	15	~15	<10	I/II? (BNO98), 11'' SW of OphA-MM2
LFAM3/GY21	<70	150	~40	110±10	flat spectrum
GSS31	65	90	~20	70±20	II
S2/GSS32	<80	70	~70	<10	II
VLA1623	940	1 000	<50	950±10	0, no ISOCAM em.
VSSG27	<20	75	>60	<20	II
S1	<15	25	~25	<10	IIID
WL8	<20	<10	none	<10	III?
WL7	<20	40	~20	(?20±10)	II, 5'' N from WLY pos.
ROC16	<25	<15	none	<15	III?
WL12	90	135	~20	115±10	I, 4.5'' N from WLY pos.
WL2	50	60	~30	(30±10)	II
VSSG3	<50	<60	none	<60	III
VSSG5	<25?	<20	none	<20	II, at ISOCAM pos.: 10'' E from VSSG pos.
WL21	<20	40	~15	(?25±10)	I/II? (BNO98), at ISOCAM pos.: (3'', 9'') from WLY pos.
WL14	<15	65	~35	?30±10	I/II? (BNO98), at ISOCAM pos.: 6'' S from GY172 pos.
WL22	30	100	~60	40±10	I, at ISOCAM pos.: 4'' S from GY174 pos.
LFAM24	<20	60	~40	?<20	Extragalactic radio source ? (BNO98), no ISOCAM em.
WL16	<10	40	~35	?<6	II, at SKS pos.
WL1	25	<20	none	<20	II
WL17	70	100	~25	75±10	II, median pos. of GY and SKS
WL10	< 30	40	~20	(20±20)	II, at ISOCAM pos.: 10'' NE from WLY pos.
EL29	100	105	~10	95±10	I, on the edge of Oph-E, protobinary ?
WL9	<30	<30	~20	<10	?
SR21	150	95	none	95±15	IID, uncertain calibration
WL11	< 20	<10	none	<10	I/II? (BNO98)
WL19	< 20	30	none	30±10	II-IIID, 5'' SW from WLY pos.
IRS34	<20	40±10	~ 30	<20	II
WL20	95	95	none	95±15	I-II Multiple source
IRS36	<20	<15	none	<15	?
IRS37	60?	25	~15	<10	II?
WL5/IRS38	35?	15	~15	<10	III
WL4/IRS39	30?	25	~10	<15	II
WL3/IRS41	30?	50	~15	(?35±20)	II; at ISOCAM pos.: 6'' S of WLY pos.
SR12A-B/IRS40	<35	30	~10	<20	III
IRS42	<35	40	none	40±20	II, near GY pos.
WL6	<25	<20	none	<20	I
IRS43	75	135	~55	80±10	I
VSSG25	<15	<10	none	<10	II
IRS44	75	70	<10	60±10	I
VSSG18	<40	200	>150	<50	II, at WLY/ISOCAM pos., 14'' SE of OphB2-MM8
IRS46	30	50	~5	45±10	I, SW from WLY pos.
VSSG17	<20	120	>100	<20	II, at WLY/ISOCAM pos., 12'' E from OphB2-MM6
IRS48	80	60	<5	60±10	I
IRS50	<20	<10	~ 10	?<10	?, confused by IRS 48
IRS51	55	120	<10	110±10	I, 4'' W from WLY pos.
IRS54	<40	30	none	(30±10)	I

## Notes to Table 5

- (1) Peak flux density in central  $11''$ -beam before background subtraction.
- (2) Background estimated using subtraction procedure described in Sect. 3.2.
- (3) Peak circumstellar flux in  $11''$ -beam estimated after background subtraction. Uncertainty mainly due to environment subtraction but also including map rms measured at source position. Values preceded by question marks correspond to tentative detections of sources confused by their environments. Weak ( $< 5\sigma$ ) detections are given in parentheses.
- (4) IID and IIID indicate double-peaked SEDs. References: BNO98 = Bontemps, Nordh, Olofsson, et al. 1998; GSS = Grasdalen, Strom, & Strom 1973; GY = Greene & Young 1992; SKS = Strom, Kepner, & Strom 1995; VSSG = Vrba et al. 1975; WLY = Wilking, Lada, & Young 1989. All sources have ISOCAM counterparts (Bontemps et al. 1998) except those indicated.

intensity of SM1 and is filtered out by the dual-beam mapping technique. In the case of the broader Oph-E core, there is a large-scale ( $> 4'$ )  $C^{18}O$  emission plateau with  $\langle N_{H_2} \rangle \sim 5 - 6 \times 10^{22} \text{ cm}^{-2}$  that amounts to as much as  $\sim 2/3$  of the peak  $C^{18}O$  intensity in the region and cannot be detected in our  $3.5'$ -size map.

On the other hand, comparison of our various bolometer coverages of Oph-C, which range from  $3'$  to  $8'$  in extent, demonstrates that dual-beam continuum observations can be sensitive to low column density material if the maps are made sufficiently large.

Dual-beam filtering can account for some of the discrepancies between the continuum and  $C^{18}O$  estimates of the core column densities (see Table 1). In the case of the compact cores Oph-A, Oph-B1, OphC-S, and Oph-D, which suffer little filtering, the continuum estimates of the peak column densities agree with the line estimates to better than a factor of  $\sim 1.8$ . The continuum estimate is 2.6 times larger than the  $C^{18}O$  estimate for Oph-B2, suggesting the  $C^{18}O$  emission may be optically thick. On the contrary, for Oph-E and Oph-F, the continuum estimates are a factor of 2.8 and 2.2 lower than the line estimates of WL83. These latter differences probably result from severe dual-beam filtering (up to a factor  $\sim 2/3$  in Oph-E, see above).

Part of the discrepancy between the continuum and  $C^{18}O$  estimates may also arise from the fact that the line estimates of WL83 and Butner et al. (1995) are based on the LTE hypothesis, while it is likely that the  $C^{18}O$  lines are *not* thermalized in the  $\rho$  Oph main core. Wilking (1992) argues that the LVG hypothesis, which yields lower column densities by a factor 1.5, may be more appropriate. If the LVG hypothesis is adopted, our continuum estimates after filtering correction become a factor  $\sim 1.2$  (Oph-F) to  $\sim 4.3$  (Oph-A) larger than the line estimates.

## References

- Abergel, A., Bernard, J.P., Boulanger, F. et al. 1996, A&A, 315, L329  
Abergel, A., André, P., Bernard, J.P. et al. 1997, in: ESA-Symposium on The Far Infrared and Submillimetre Universe, Grenoble, p. 247 (ESA SP-401)  
Adams, F.C., Lada, C.J., & Shu, F.H. 1987, ApJ, 312, 788  
André, P. 1996, In: M. Rodonò & S. Catalano (eds.) Highlights of European Astrophysics (JENAM-95), Mem.S.A.It., Vol.67, No.4, p. 901  
André, P., Montmerle, T. 1994, ApJ 420, 837 (AM94)  
André, P., Montmerle, T., & Feigelson, E. D., Stine, P.C., & Klein, K.L. 1988, ApJ, 335, 940  
André, P., Ward-Thompson, D., Barsony, M. 1993, ApJ, 406, 122 (AWB93)  
André, P., Ward-Thompson, D., & Motte, F. 1996, A&A, 314, 625 (AWM96)  
Bacmann, A., André, P., Abergel, A. et al. 1998, in Star Formation with ISO, Proc. of Lisbon Meeting (June 1997), J.L. Yun & R. Liseau (eds.), ASP 132, p. 307  
Barsony, M., Kenyon, S.J., Lada, E.A., Teuben, P.J. 1997, ApJS, 112, 109  
Bastien, P., Arcoragi, J.-P., Benz, W., Bonnell, I., & Martell, H. 1991, ApJ, 378, 255  
Basu, S. 1997, ApJ, 485, 240  
Beckwith, S.V.W., Sargent A.I, Chini, R.S., Guesten, R. 1990, AJ, 99, 924  
Blitz, L. 1993, in *Protostars and Planets III* p. 125, eds. E.H. Levy & J.I. Lunine (The University of Arizona Press, Tucson)  
Bohlin, R.C., Savage, B.D., & Drake, J.F. 1978, ApJ, 224, 132  
Bonnell, I.A., Bate, M.R., Price, N.M. 1996, MNRAS, 279, 121  
Bonnor, W.B. 1956, MNRAS, 116, 351  
Bontemps, S., Nordh, L., Olofsson, G., et al. 1998, in prep.  
Boss, A.P. 1995, ApJ 439,223  
Brogière, D., Neri, R., & Sievers, A. 1995, NIC bolometer users guide (IRAM internal report)  
Butner, H.M., Lada, E.L., Loren, R.B. 1995, 448, 207  
Carlberg, R.G., Pudritz, R.E. 1990, MNRAS, 247, 353  
Calvet, N., Hartmann, L., Kenyon, S.J., & Whitney, B.A. 1994, ApJ, 434, 330  
Casanova, S., Montmerle, T., Feigelson, E.D., & André, P. 1995, ApJ, 439, 752  
Cesarsky, D., Lequeux, J., Abergel, A., Péroul, M., Palazzi, E., Madden, S., & Tran, D. 1996, A&A, 315, L309  
Chini, R., Reipurth, B., Ward-Thompson, D., Bally, J., Nyman, L.A., Sievers, A., & Billawala, Y. 1997, ApJ, 474, L135  
Ciolek, G.E., & Mouschovias, T.Ch. 1994, ApJ, 425, 142  
Comerón, F., Rieke, G.H., Burrows, A., & Rieke, M.J. 1993, ApJ, 416, 185 (CRBR)  
de Geus, E.J. 1992, A&A, 262, 258  
Elmegreen, B.G., Elmegreen, D.M. 1978, ApJ, 220, 1051  
Emerson, D.T., Klein, U., & Haslam, C.G.T. 1979, A&A, 76, 92  
Emerson, J.P. 1996, in: Siebenmorgen, R., Kaufl, H.U. (eds.) The Role of Dust in the Formation of Stars. ESO Astrophysics Symposia, p. 19  
Emerson, J.P., Moore, T.J.T., Skinner, C.J., & Meixner, M.M. 1996, in: Siebenmorgen, R., Kaufl, H.U. (eds.) The Role of Dust in the Formation of Stars. ESO Astrophysics Symposia, p. 23  
Foster, P.N., Chevalier, R.A. 1993, ApJ 416,303

- Foster, P.N., Boss, A.P. 1996, *ApJ* 468, 784
- Gomez, M., Hartmann, L., Kenyon, S.J., & Hewett, R. 1993, *AJ*, 105, 1927
- Goodman, A.A., & Heiles, C. 1994, *ApJ*, 424, 208
- Greene, T.P., & Young, E.T. 1992, *ApJ*, 395, 516 (GY)
- Greene, T.P., & Meyer, M.R. 1995, *ApJ*, 450, 233
- Greene, T.P., Wilking, B.A., André, P., Young, E.T., & Lada, C.J. 1994, *ApJ*, 434, 614 (GWAYL)
- Griffin, M.J., & Orton, G.S. 1993, *Icarus*, 105, 337
- Güsten, R., & Mezger, P.G. 1983, *Vistas in Astronomy*, 26, 159
- Henning, Th., Michel, B., & Stognienko, R. 1995, *Planet. Space Sci.* (Special issue: Dust, molecules and backgrounds), 43, 1333
- Henriksen, R.N., André, P., & Bontemps, S., 1997, *A&A*, 323, 549
- Kenyon, S.J., Calvet, N., Hartmann, L. 1993, *ApJ*, 414, 676
- Kreysa, E. 1992, in: *ESA-Symposium on Photon Detectors for Space Instrumentation*, Noordwijk, p. 207 (ESA SP-356)
- Lada, C.J. 1987, in: *Star Forming Regions*, IAU 115, p. 1
- Lada, E.A., Strom, K.M., & Myers, P.C. 1993, in *Protostars & Planets III*, p. 245
- Ladd, E.F., Adams, F.C., Casey, S. et al. 1991, *ApJ*, 382, 555
- Langer, W.D., Wilson, R.W., & Anderson, C.H. 1993, *ApJ*, 408, L45
- Langer, W.D., Velusamy, T., Kuiper, T.B.H., Levin, S., Olsen, E., & Migenes, V. 1995, *ApJ*, 453, 293
- Larson, R.B. 1969, *MNRAS*, 145, 271
- Larson, R.B. 1985, *MNRAS*, 214, 379
- Leous, J.A., Feigelson, E.D., André, P., & Montmerle, T. 1991, *ApJ*, 379, 683 (LFAM)
- Loren, R.B. 1989, *ApJ*, 338, 902
- Loren, R.B., Wootten, A. 1986, *ApJ*, 306, 142
- Loren, R.B., Wootten, A., Wilking, B.A. 1990, *ApJ*, 365, 229 (LWW90)
- Loren, R.B., Sandqvist, A., Wootten, A. 1983, *ApJ*, 270, 620
- Loren, R.B., Wootten, A., Sandqvist, A., Bernes, C. 1980, *ApJ*, 240, L165
- Meyers, K.A., Snow, T.P., Federman, S.R., Breger, M. 1985, *ApJ*, 288, 148
- Mezger, P.G., Chini, R., Kreysa, E., Wink, J.E., Salter, C.J. 1988, *A&A*, 191, 44
- Mezger, P.G., Sievers, A., Haslam C.G.T., Kreysa, E., Lemke, R., Mauersberger, R., & Wilson, T.L. 1992a, *A&A*, 256, 631
- Mezger, P.G., Sievers, A., Zylka, R., Haslam C.G.T., Kreysa, E., Lemke, R. 1992b, *A&A*, 265, 743
- Miller, G.E., Scalo, J.M. 1979, *ApJS*, 41, 513
- Montmerle, T., Koch-Miramond, L., Falgarone, E., & Grindlay, J. E. 1983, *ApJ*, 269, 182
- Motte, F., André, P., Neri, R. 1996, in: *Siebenmorgen, R., Kaufl, H.U. (eds.) The Role of Dust in the Formation of Stars. ESO Astrophysics Symposia*, p. 47
- Motte, F., André, P., et al. 1998, in prep.
- Mouschovias, T.Ch. 1991, in: *The Physics of Star Formation and Early Stellar Evolution*, Eds. Lada & Kylafis, p. 449
- Nordh, L., Olofsson, G., Abergel, A. et al. 1996, *A&A*, 315, L185
- Ossenkopf, V., Henning, Th. 1994, *A&A*, 291, 943
- Pollack, J.B., Hollenbach, D., Beckwith, S., Simoneli, D.P., Roush, T., Fong, W., 1994, *ApJ*, 421, 615
- Pound, M.W., Blitz, L. 1993, *ApJ*, 418, 328
- Pound, M.W., Blitz, L. 1995, *ApJ*, 444, 270
- Preibisch, Th., Ossenkopf, V., Yorke, H.W., & Henning, Th. 1993, *A&A*, 279, 577
- Ristorcelli, I., Serra, G., et al. 1997, *IRTS symposium*, Tokyo, in press
- Salpeter, E.E. 1955, *ApJ*, 121, 161
- Sato, S., Tamura, M., Nagata, T., Kaifu, N., Hough, J., McLean, I.S., Garden, R.P., Gatley, I. 1988, *MNRAS*, 230, 321
- Scalo, J.M. 1986, *Fund. Cosmic Phys.*, 11, 1
- Schlickeiser, R., Harwit, M., Özel, M.E., Sieber, W., Younis, S.M., & Schinkel, A. 1989, *A&A*, 216, 197
- Schneider, S., Elmegreen, B.G. 1979, *ApJS*, 41, 87
- Schwartz, P.R., Snell, R.L., Schloerb, F.P. 1989, *ApJ*, 336, 519
- Shu, F.H., Adams, F.C., Lizano, S. 1987, *ARA&A* 25, 23
- Starck, J.L., Bijaoui, A., & Murtagh, F. 1995, in *CVIP: Graphical Models and Image Processing*, 57, 5, 420
- Strom, K.M., Strom, S.E., & Merrill, K.M. 1993, *ApJ*, 412, 233
- Strom, K.M., Kepner, J., Strom, S.E. 1995, *ApJ*, 438, 488
- Terebey, S., Chandler, C.J., & André, P. 1993, *ApJ*, 414, 759
- Tomisaka, K. 1996, *PASJ*, 48, L97
- Troland, T.H., Crutcher, R.M., Goodman, A.A., Heiles, C., Kazès, I., & Myers, P.C. 1996, 471, 302
- Vrba, F.J. 1977, *AJ*, 82, 198
- Vrba, F.J., Strom, K., Strom, S.E., & Grasdalen, G.L. 1975, *ApJ*, 197, 77
- Walker, C.K., Adams, F.C., & Lada, C.J. 1990, *ApJ*, 349, 515
- Walter, F.M., Vrba, F.J., Mathieu, R.D., Brown, A., & Myers, P.C. 1994, *AJ*, 107, 692
- Ward-Thompson, D., Scott, P.F., Hills, R.E., & André, P. 1994, *MNRAS*, 268, 276
- Wilking, B.A. 1992, in *ESO Sci. Rep.*, No. 11, *Low Mass Star Formation in Southern Molecular Clouds*, ed. B. Reipurth, 159
- Wilking, B.A., & Lada, C.J. 1983, *ApJ*, 274, 698 (WL83)
- Wilking, B.A., Lada, C.J., & Young, E.T. 1989, *ApJ*, 340, 823 (WLY)
- Whitworth, A.P., Bhattal, A.S., Chapman, S.J., Disney, M.J., & Turner, J.A. 1994 *MNRAS*, 268, 291
- Woodward, P.R. 1978, *ARA&A* 16, 555
- Zinnecker, H. 1989, in: *Evolutionary phenomena in Galaxies*, eds. J.E. Beckman and B.E.J. Pagel (Cambridge: Cambridge University Press), p. 113